The Astronomical Journal, 163:78 (19pp), 2022 February https://doi.org/10.3847/1538-3881/ac3762


# On the Same Wavelength as the Space Telescope Imaging Spectrograph

Thomas R. Ayres
Center for Astrophysics and Space Astronomy, 389 UCB, University of Colorado, Boulder, CO 80309, USA; Thomas.Ayres@Colorado.edu
*Received 2021 September 24; revised 2021 November 2; accepted 2021 November 6; published 2022 January 20*

## Abstract

The Hubble Space Telescope Imaging Spectrograph (STIS) is a powerful tool for high spectral resolution ultraviolet (UV; 1150–3200 Å) studies of bright cosmic sources. However, achieving the superb wavelength precision inherent in its UV echelle channels is hampered by subtle camera distortions that are not fully compensated for by the CALSTIS pipeline. The systematics arise from the low-order ($n = 2$) bivariate polynomial dispersion model employed in the echellegram processing. The formulation does remarkably well given its simplicity (only seven terms in the current implementation), but cannot account for apparent higher frequency undulations in the STIS spectral images. Previous correction schemes have built elaborate distortion maps, with up to thirty-six terms, operating on the individual echelle orders in the pipeline "x1d" file, prior to merging the orders. There is, however, a more straightforward, although partial, solution: a polynomial formula in the wavelength domain applied to the order-merged spectrum; just $n = 3$ for most of the STIS settings, although up to $n = 5$ for a few of the more recalcitrant ones.

*Unified Astronomy Thesaurus concepts:* Astronomical instrumentation (799); Spectrometers (1554); Calibration (2179); Spectral line identification (2073)

*Supporting material:* figure set

## 1. Introduction

Space Telescope Imaging Spectrograph (STIS) is one of the complement of four experiments in the axial bay of Hubble Space Telescope (HST). STIS is a multichannel instrument with numerous direct imaging, spectroscopic, and long-slit stigmatic spectroscopy modes. Perhaps best known is STIS's cross-dispersed ultraviolet (UV) echelle system. It operates in both the far-ultraviolet (FUV: 1150–1700 Å) and near-ultraviolet (NUV: 1700–3200 Å), with separate Multi-Anode Microchannel Array (MAMA) cameras; in medium resolution (M: $\lambda/\Delta\lambda \sim 30{,}000$–$45{,}000$) and high resolution (H: 110,000). STIS was installed in Hubble in 1997 and ran prolifically until 2004, but then was rendered inoperable by a power-supply failure. STIS was restored to working order in 2009 thanks to Servicing Mission 4 (SM4).

The UV echelle channels of STIS are popular, having accumulated more than 6,000 exposures of about 1000 distinct targets. Recent studies with the STIS echelles include: chemical compositions of nearby Sirius (Castelli et al. 2017), the nonmagnetic B star HR 6000 (Cowley et al. 2016), and uranium-rich, metal-poor CS 31082-001 (Siqueira-Mello et al. 2016); ISM properties in lines of sight toward the Voyager interplanetary probes (Zachary et al. 2018); high-precision masses and distances of Cepheids from UV radial velocities of companions (Gallenne et al. 2018); fundamental characteristics of hot stars in Orion (Richardson et al. 2015) and globular cluster M3 (Chayer et al. 2015); outflowing multiphase gas in the Galactic halo (Savage et al. 2017); ISM thermal pressures in the SMC and LMC (Welty et al. 2016), as well as abundances and depletions (Jenkins & Wallerstein 2017; Roman-Duval et al. 2019); the circumgalactic medium around nearby galaxies (Keeney et al. 2017); active galactic nucleus outflows (Denes Couto 2017); energy levels of Mn II (Castelli et al. 2015) and Fe I (Peterson & Kurucz 2015); and the gravity dependence of the fine-structure constant, $\alpha$, based on white dwarf spectra (Bainbridge et al. 2017).

In some studies, such as of the ionizing radiation fields of planet-hosting K and M dwarfs by France et al. (2016) and FUV molecular emissions from protoplanetary disks by Hoadley et al. (2017), STIS captured the brighter members of a sample, whereas sister HST instrument Cosmic Origins Spectrograph recorded the fainter ones.

These few examples by no means exhaust the diversity of projects undertaken with the STIS UV echelles over the past two and a half decades.

Figure 1 illustrates the cross-dispersed echelle format.[1] The example image is a raw wavelength calibration exposure ("wavecal") from the heavily used FUV medium-resolution setting E140M-1425. Intensities are depicted in reverse gray scale; wavelengths range from ∼1150 Å, at the bottom of the frame, to ∼1720 Å at the top. The small dark spots (actually, rectangles) are individual emission lines from the Pt/Ne-Cr hollow cathode lamp, as imaged through a narrow, short slit. Thin, nearly horizontal, bands trace the echelle orders, $m$, numbered along the right-hand axis (for the even ones). Each order is about a dozen Å wide in the $x$-direction, with wavelengths increasing from left to right. The orders overlap at their ends, more so at the bottom of the format (smaller wavelengths) than at the top. For example, the pattern of dots at the right side of order 119 repeats at the left side of the next order up ($m = 118$).

As a natural evolution of the use of the same instrument over a quarter century, investigators increasingly are working at the limits of STIS's photometric and wavelength precision. Nevertheless, pushing the instrumental wavelength precision



[1] The echelle grating, operated in high order, creates a series of high-resolution spectral slices, in the $x$-direction, that degenerately fall on top of one another. A low-resolution cross-disperser grating then separates the orders in the $y$ direction.

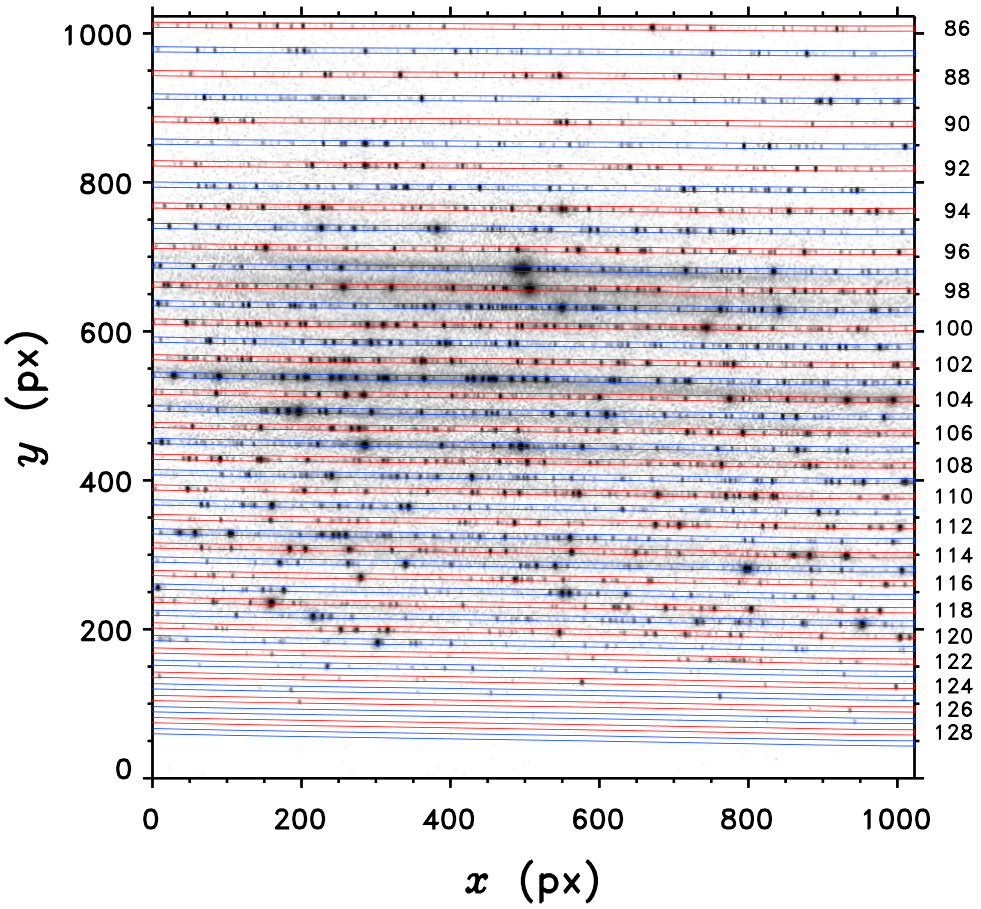


**Figure 1.** Example STIS wavecal echellegram from FUV medium-resolution setting E140M-1425. Slightly slanted bands highlight the individual echelle orders: red for even $m$ (numbered at right), blue for odd.

has revealed subtle distortions in the echelle dispersion properties that are not fully compensated for in the standard CALSTIS pipeline processing (Ayres 2010a). The mismatch devolves from the relatively low-order bi-quadratic polynomials used to assign wavelengths to pixel numbers.[2] Fortunately, the distortions are straightforward to characterize, if wavelength calibrations of suitable quality are available: namely, deep exposures of the Pt/Ne-Cr hollow cathode lamps to achieve high line densities across the echelle format. Derived corrections can been applied directly to the CALSTIS pipeline output (so-called "x1d" file, a tabulation of fluxes, wavelengths, and photometric errors, for each of up to several dozen echelle orders) to compensate for the residual wavelength errors (see Ayres 2010a).

An example is the Advanced Spectral Library (ASTRAL[3]), which hosts STIS UV echelle spectra, mostly full coverage, of about forty bright stars, representing early and late types; several metal deficient turn-off stars and related objects (NUV, only); and two extensively monitored white dwarfs from the STIS photometric calibration program. The main feature of the custom processing for ASTRAL was an advanced wavelength scale correction, building on the earlier "StarCAT" effort (Ayres 2010a). The most recent version of the ASTRAL protocols utilized all of the deep-exposure wavecals acquired up to circa 2016, including special purpose Guest Observer calibration programs (e.g., GO-12280: "Deep Lamp Too"). ASTRAL leveraged newly updated line lists (mainly from the National Institute of Standards and Technology, or NIST), especially for Cr I and Cr II. Chromium had been incorporated in the flight lamps of STIS (and its predecessor, Goddard High-Resolution Spectrograph (GHRS: 1990–1997)) to bolster the line densities, especially in the NUV, compared with earlier devices flown on IUE.

The ASTRAL Project utilized the extensive collection of wavecal echellegrams to recalculate dispersion coefficients in the bivariate formula employed by CALSTIS, for all of the 44 supported echelle CENWAVEs of STIS. A high-order $m$-dependent polynomial model was developed in parallel to correct any systematic residuals between the new dispersion model and the measured lamp wavelengths. The correction formula could be applied to the $m$-resolved x1d file of an external target exposure (say, a star), prior to merging the overlapping wavelengths of the echellegram. The ASTRAL

[2] For heritage reasons, dating back to the pioneering echelle spectrograph of the International Ultraviolet Explorer (IUE: 1978–1996), the CALSTIS dispersion model is described as $x = f(m, \lambda)$, where $x$ is the horizontal pixel coordinate and $f = D_0 + D_1\, m\lambda + D_2\, m^2\lambda^2 + D_3\, m + D_4\, \lambda + D_5\, m^2\lambda + D_6\, m\lambda^2$, for wavelength $\lambda$ and echelle order $m$. The $D_i$ are the "dispersion coefficients" (seven altogether). Note that terms in $\lambda^2$ and $m^2$ are missing, which otherwise would have constituted a complete set. Further, $m$ and $\lambda$ are not properly orthogonal variables, because the hybrid variable $k = m\lambda$ ("grating parameter") varies exclusively along the orders, whereas $\lambda$ and $m$, independently, have power in the cross-dispersion direction. Wavelengths are assigned to the $x$ pixels in echelle order $m$ by solving the associated quadratic for $\lambda$.

[3] https://casa.colorado.edu/~ayres/ASTRAL/

correction model still is the gold standard, but it is complex, with up to several dozen terms needed for some of the more affected settings. Further, the ASTRAL distortion maps are less well defined for CENWAVEs where the coverage of the lamp lines is sparse, owing to either properties of the atomic emission spectra —the line densities fall off rapidly toward shorter wavelengths in the FUV (e.g., Figure 1)—or limited exposure depth in the archival collection of wavecals for that setting.[4]

In hindsight, the ASTRAL wavelength correction scheme was overly elaborate. Further, the evolving nature of the CALSTIS reference files, especially with regard to photometric calibrations, motivates the desire to have a correction that can be applied directly to the standard CALSTIS pipeline output, as disgorged by the on-the-fly (OTF) calibration system in the MAST archive,[5] rather than the custom version of the pipeline and reference files utilized by ASTRAL.

There was another wrinkle. During the initial STIS operational period, 1997 February to 2002 August, the home set positions on the Grating Wheel ("Mode Select Mechanism," or MSM) were shifted monthly by small amounts in an effort to avoid prematurely aging the MAMA detectors at locations of bright echelle orders (for example, from UV continuum sources like hot stars).[6] It is not clear whether the periodic shifts helped smooth out the microchannel plate scrubbing, but they did cause unintended side effects for the usability of the routine wavelength calibrations (which might be taken at different MSM offsets for the same nominal CENWAVE). That was because the MSM displacements translated, and slightly rotated, the spectrum diagonally on the detector, so the impact on the wavelengths was nonlinear. Some compensation for these effects was built into the pipeline processing, but the outcome then became dependent on additional parameters. Thankfully, the STIS team decided mid-2002 to freeze the MSM home positions of the echelle settings,[7] a positive step toward ensuring consistent wavelengths for those modes. As of early 2020, however, only about half of the 44 echelle CENWAVEs had suitable lamp observations at the new encoder positions post-SM4 (noting that the five-year cold-storage of the instrument might also have subtly affected the dispersion properties).

The lack of post-SM4 wavecals for many STIS settings was addressed in Cycle 27 Guest Observer program GO-15948 ("Make STIS Great Again!"), which obtained deep lamp exposures in 21 under-observed settings. Concurrently, a strategy was devised to simplify the wavelength distortion corrections previously developed for ASTRAL. The new approach took advantage of the fact that the major deviations in the wavelength residuals typically (but not always) were in the cross-dispersion direction (i.e., the major wavelength axis, perpendicular to the echelle stripes), rather than from one side of an echelle order to the other. Thus, a modest-order polynomial in wavelength could remove much of the residual distortions from a merged version of the pipeline x1d file (i.e., concatenating the partially overlapping echelle orders into a coherent 1D spectrum, using a suitable averaging scheme, say involving tapered weighting functions, as in the ASTRAL protocols, to blend together the overlaps). As mentioned above, because the new correction was layered on top of the dispersion solution already in the pipeline, there was no need to upgrade the dispersion coefficients currently in place. At the same time, if the CALSTIS dispersion coefficients are repopulated at a future date, the infrastructure would be in place to reconstitute a post-pipeline correction to match. Finally, unlike the order-resolved ASTRAL approach, the new simplified scheme is not affected by the spatial distribution of the lamp emission lines on the detector in the $x$-dimension, and only relies on having a sufficient density of lines in the wavelength domain to define the correction.

## 2. Observations

Table 1 lists the new wavecals obtained by GO-15948 as an example of the quality of calibration material now available. Integration times for that program were set to build up adequate depth for the CENWAVEs lacking sufficient prior exposures, or in some cases (especially the shorter exposures (<1 ks) in Table 1), to supplement otherwise adequate pre-SM4 material with at least one post-SM4 reference exposure. Table 2 summarizes, in a more schematic way, the totality of deep ($t_{\rm exp} > 100$ s) wavecals for all 44 supported STIS settings. The calibrations are divided into pairs: one for the initial STIS operational period (1997–2004), and a second for post-SM4 (2009–present). The reason for the separation was mentioned earlier. The post-SM4 instrument properties are most appropriate for deriving dispersion relations and wavelength correction models, not only given the stable MSM positions (which were in place from 2002 August to 2004 August as well), but also because of the large number of STIS echelle exposures obtained over the more than a decade since the instrument was recovered during SM4. The stable MSM set positions ensure that the lamp lines always fall on essentially the same pixels (the repositioning of the mechanism is accurate to a few pixels in $x$ and $y$ versus the typical order widths (in $y$) of about 7 pixels), so the wavecals are always seeing roughly the same camera distortions (rather than moving relative to them as in the pre-2002 era). For that reason, the post-SM4 data sets were adopted as the fundamental reference.

Several of the NUV E230H (NUV-H) settings have two observation slits listed. Normally, a special aperture ($0\farcs1 \times 0\farcs09$ (height × width), hereafter $0.1 \times 0.09$) was used for the NUV-H wavecals, to avoid blending the orders on the short-wavelength side of the echelle format where they are more crowded, especially for the NUV settings with CENWAVEs below 1900 Å. However, the emission lamps have faded in brightness over the years, and the $0.1 \times 0.09$ aperture passes only half the light as the $0.2 \times 0.09$ slit,[8] the default

[4] This issue is more apparent in the less frequently used secondary settings, because they tend to be less well calibrated than the recommended primary CENWAVEs. Nevertheless, there are situations when a secondary setting is needed to bridge an insufficient overlap between two adjacent primaries (such as NUV E230H-2762 and E230H-3012, for which technically the cross-over is only 1 Å wide; Table 2), or between NUV M resolution and H resolution for steep UV photospheric continua (for example, the long-wavelength end of M primary E230M-1978 misses the short-wavelength edge of H primary E230H-2513 by more than 10 Å (Table 2, below), so secondary setting E230H-2463 is needed to cover the gap, as commonly was done for the ASTRAL hot stars). Bridging the cases of too narrow overlaps or outright gaps is important to enable the bootstrapping of relative velocity and flux calibrations across a spectrum composed of several independent segments, according to spectral features in the overlap zones of the neighboring segments (for the velocity part) as well as the joint intensity levels themselves (for the flux part).

[5] https://archive.stsci.edu/hst/search.php

[6] A less extreme version of the lifetime position shifts for HST's Cosmic Origins Spectrograph.

[7] The MSM shifts continue to be done for the first-order gratings, where the impact on the processed wavelength scales is minimal.

[8] The wavecal lamps diffusely illuminate the slit plane, so count rates are proportional to the slit area.

**Table 1**
New STIS Wavecal Spectra from GO-15948

| ObsID | UT Start (yyyy-mm-dd) | Setting | $t_{exp}$ (ks) |
|---|---|---|---|
| (1) | (2) | (3) | (4) |
| oe1610010 | 2020-04-06 | E140H-1307 | 1.4 |
| oe1611010 | 2020-06-01 | E140H-1453 | 1.7 |
| oe1630010 | 2020-06-01 | E230H-1813 | 1.4 |
| oe1631010 | 2020-06-01 | E230H-1863 | 1.1 |
| oe1632010 | 2020-06-01 | E230H-1913 | 1.4 |
| oe1640010 | 2020-06-01 | E230H-2013 | 1.2 |
| oe1620010 | 2020-04-06 | E230M-2124 | 1.1 |
| oe1642010 | 2020-06-02 | E230H-2263 | 1.6 |
| oe1621010 | 2020-04-06 | E230M-2269 | 1.4 |
| oe1643cbq | 2020-05-25 | E230H-2313 | 0.3 |
| oe1660010 | 2020-06-02 | E230H-2363 | 1.1 |
| oe1661010 | 2020-06-02 | E230H-2413 | 1.1 |
| oe1662czq | 2020-05-25 | E230H-2463 | 0.5 |
| oe1644010 | 2020-05-25 | E230H-2513 | 0.9 |
| oe1643ccq | 2020-05-25 | E230H-2563 | 0.25 |
| oe1650010 | 2020-06-01 | E230H-2663 | 1.1 |
| oe1622010 | 2020-04-06 | E230M-2707 | 1.6 |
| oe1641010 | 2020-06-01 | E230H-2762 | 1.2 |
| oe1662d0q | 2020-05-25 | E230H-2812 | 0.5 |
| oe1663010 | 2020-06-02 | E230H-2862 | 1.1 |
| oe1651010 | 2020-06-02 | E230H-3012 | 1.2 |

**Note.** Col. 1 is the STIS data set name. Col. 2 is the UT start date of the exposure. Col. 3 is the echelle setting: "140" series are FUV; "230" are NUV; M is medium resolution; H is high resolution; trailing number is the central wavelength (CENWAVE: Å). Col. 4 is the integration time in kiloseconds (ks). All of the NUV-H exposures were taken through the $0\farcs2 \times 0\farcs09$ slit (hereafter, $0.2 \times 0.09$). Normally, a special slit, $0.1 \times 0.09$, is used for NUV-H wavelength calibrations, but substitution of the standard science spectroscopic slit, $0.2 \times 0.09$, approximately doubled the signal levels, which is important given the fading lamp output in recent years. The FUV-H exposures also utilized the $0.2 \times 0.09$ slit, while the lone NUV-M observation used the $0.2 \times 0.06$ slit, the default spectroscopic aperture for that mode.

employed in NUV-H studies of external objects, like stars, for the best resolution and throughput. To achieve adequate signal-to-noise ratios (S/N) while also conserving lamp longevity, the new NUV-H wavecals were taken with the $0.2 \times 0.09$ slit. In fact, even with the taller slit, order crowding was not an issue at the shortward ends of the NUV-H settings with CENWAVEs $<1900$ Å.

## 3. Analysis

The large collection of STIS wavecals was processed through the standard CALSTIS pipeline (a departure from ASTRAL, which utilized custom reference files), whose primary output is the so-called "x1d" data product. The notional scheme first merged the orders of the wavecal x1d data set into a 1D spectrum, then measured the apparent lamp line positions as a function of wavelength. (The reverse of what was done in the earlier order-resolved implementation for ASTRAL. There, the lines were measured as a function of $\lambda$ in each separate order $m$ of the x1d file, oblivious to any wavelength overlaps between adjacent orders.)

In practice, the line position measurements were carried out in co-added 1D spectra, accumulated from all of the available deep wavecal exposures of each setting. The co-additions were done separately for the pre- and post-SM4 data sets of a given CENWAVE. Then, the pair of co-adds was combined, adopting the post-SM4 realization as the reference, and adjusting the zero-point of the pre-SM4 spectrum to match by cross-correlation. Inevitably, some of the pre-2002 wavecals were taken at nonstandard MSM positions (with respect to the post-SM4 era), so the corrections applied by CALSTIS for these offsets came into play. In most cases, any small deviations introduced by an insufficient correction for the offset MSM rotations by the pipeline were countered by the fact that the subsequent post-SM4 exposure depths often exceeded those of the pre-2002 collections.

A specialized emission line measurement strategy—using a pseudo-Gaussian formulation (see Ayres et al. 2021) appropriate for variable profile shapes—was applied to the super-co-add of each CENWAVE (as enumerated in Table 2). Empirically, many of the STIS lamp emissions had sub-Gaussian profiles, namely with the normal Gaussian exponent $a = 2$ replaced by smaller values, typically $a \sim 1.5$. A sub-Gaussian profile has a narrower core and broader wings than a pure Gaussian, and apparently better matches the intrinsic echelle instrumental profiles for bright lamp lines (which have sharp cores with Lorentzian scattering wings, whose amplitude varies with wavelength; STIS Instrument Handbook,[9] Figure 13.92 (M resolution) and Figure 13.93 (H)). However, more Gaussian shapes can be found among the weaker lines for which the low-amplitude scattering wings are lost in the background photometric noise; and occasionally super-Gaussian profiles (more rounded than a pure Gaussian) were seen as well. The key point is that the wavelength measurement was based on fitting the profile that best matched the empirical line shape, rather than a more approximate one had the model been forced to be a pure Gaussian.

Figures 2(a) and (b) illustrate examples of the co-added STIS lamp spectra, for the FUV and NUV, respectively. Note the logarithmic scales, which span several orders of magnitude in intensity to accommodate the weak and strong lamp features. The tracings were truncated on the low-intensity side by a heavily smoothed $1\sigma$ photometric noise level, which appears as an undulating pseudo-continuum. The numerous sharp, sometimes blended, lamp emissions above that background come mainly from ionized platinum, chromium, and neon. The two metals were incorporated in the hollow cathode of the discharge lamp. Neon is the buffer gas, although minor contaminants—hydrogen, oxygen, and carbon—are also present. The roughly horizontal wavy dotted line represents a photometric S/N threshold, to decide whether or not to measure a particular emission feature, set so that the precision of the wavelength would be comparable to, or better than, 0.3 km s$^{-1}$. This limit ($\frac{1}{20}$ of a spectral resolution element (resel) for M-mode and $\frac{1}{10}$ resel for H) maximized the number of suitable target lines, while minimizing the inaccuracy of the measurements with respect to the laboratory wavelengths (which had an imposed accuracy of $\lesssim$0.2 km s$^{-1}$).

Identifications from NIST[10] are provided for emissions that exceeded the S/N limit. Vertical dark dotted lines mark features that were eliminated from consideration owing to close blends or asymmetries. The laboratory wavelengths are the NIST "Ritz" values, determined from energy-level differences,

[9] see https://hst-docs.stsci.edu/stisihb/.

[10] Kramida, A., Ralchenko, Yu., Reader, J., and NIST ASD Team (2020). NIST Atomic Spectra Database (ver. 5.8), (Online: https://physics.nist.gov/asd 2021). National Institute of Standards and Technology, Gaithersburg, MD. DOI: 10.18434/T4W30F.

**Table 2**
Summary of Deep Wavecal Spectra

| Setting | λ Range (Å) | 1997–2004 Slit (″) × (″) | 1997–2004 N | 1997–2004 $t_{TOT}$ (ks) | 1997–2004 $t_{min}$–$t_{max}$ (s) | 2009–Present Slit (″) × (″) | 2009–Present N | 2009–Present $t_{TOT}$ (ks) | 2009–Present $t_{min}$ − $t_{max}$ (s) |
|---|---|---|---|---|---|---|---|---|---|
| (1) | (2) | (3) | (4) | (5) | (6) | (7) | (8) | (9) | (10) |
| **FUV Medium Resolution** | | | | | | | | | |
| *E140M-1425* | 1140–1729 | 0.2 × 0.06 | 12 | 9.66 | 663–1450 | 0.2 × 0.06 | 13 | 8.23 | 620–663 |
| **FUV High Resolution** | | | | | | | | | |
| *E140H-1234* | 1141–1335 | 0.2 × 0.09 | 3 | 2.10 | 524–1048 | 0.2 × 0.09 | 6 | 8.60 | 550–4050 |
| E140H-1271 | 1160–1356 | 0.2 × 0.09 | 9 | 11.13 | 797–3600 | 0.2 × 0.09 | 13 | 6.62 | 400–865 |
| E140H-1307 | 1196–1397 | 0.2 × 0.09 | 2 | 1.80 | 600–1200 | 0.2 × 0.09 | 7 | 3.20 | 300–1400 |
| E140H-1343 | 1242–1440 | 0.2 × 0.09 | 2 | 0.70 | 311–386 | 0.2 × 0.09 | 13 | 8.56 | 550–1800 |
| E140H-1380 | 1280–1475 | 0.2 × 0.09 | 1 | 0.31 | 308 | 0.2 × 0.09 | 1 | 2.60 | 2600 |
| *E140H-1416* | 1316–1517 | 0.2 × 0.09 | 9 | 3.13 | 266–1000 | 0.2 × 0.09 | 19 | 7.55 | 266–500 |
| E140H-1453 | 1359–1551 | 0.2 × 0.09 | 1 | 0.24 | 236 | 0.2 × 0.09 | 1 | 1.70 | 1700 |
| E140H-1489 | 1390–1586 | 0.2 × 0.09 | 1 | 0.24 | 241 | 0.2 × 0.09 | 1 | 2.60 | 2600 |
| E140H-1526 | 1428–1622 | 0.2 × 0.09 | 2 | 0.62 | 272–348 | 0.2 × 0.09 | 2 | 2.30 | 300–2000 |
| E140H-1562 | 1463–1661 | 0.2 × 0.09 | 1 | 0.34 | 344 | 0.2 × 0.09 | 1 | 2.60 | 2600 |
| *E140H-1598* | 1494–1687 | 0.2 × 0.09 | 10 | 8.56 | 361–3600 | 0.2 × 0.09 | 12 | 4.80 | 400–401 |
| **NUV Medium Resolution** | | | | | | | | | |
| *E230M-1978* | 1610–2365 | 0.2 × 0.06 | 9 | 3.23 | 190–950 | 0.2 × 0.06 | 11 | 2.37 | 190–260 |
| E230M-2124 | 1691–2509 | 0.2 × 0.06 | 2 | 0.30 | 140–159 | 0.2 × 0.06 | 2 | 2.00 | 900–1100 |
| E230M-2269 | 1861–2672 | 0.2 × 0.06 | 3 | 0.33 | 110 | 0.2 × 0.06 | 1 | 1.40 | 1400 |
| E230M-2415 | 1989–2819 | 0.2 × 0.06 | 2 | 0.26 | 127–135 | 0.2 × 0.06 | 12 | 2.38 | 135–900 |
| E230M-2561 | 2135–2939 | 0.2 × 0.06 | 2 | 0.61 | 109–500 | 0.2 × 0.06 | 11 | 1.32 | 120 |
| *E230M-2707* | 2280–3118 | 0.2 × 0.06 | 2 | 1.90 | 950 | 0.2 × 0.06 | 1 | 1.60 | 1600 |
| **NUV High Resolution** | | | | | | | | | |
| *E230H-1763* | 1629–1901 | 0.1 × 0.09 | 5 | 3.36 | 411–1712 | 0.1 × 0.09 | 11 | 9.28 | 800–920 |
| E230H-1813 | 1679–1954 | 0.1 × 0.09 | 6 | 4.43 | 739 | 0.2 × 0.09 | 1 | 1.40 | 1400 |
| E230H-1863 | 1728–2000 | 0.1 × 0.09 | 2 | 1.37 | 673–698 | 0.1, 0.2 × 0.09 | 2 | 2.00 | 900–1100 |
| E230H-1913 | 1780–2053 | 0.1 × 0.09 | 2 | 1.74 | 578–1164 | 0.2 × 0.09 | 1 | 1.40 | 1400 |
| E230H-1963 | 1831–2103 | 0.1 × 0.09 | 1 | 0.52 | 521 | 0.1 × 0.09 | 12 | 10.22 | 800–930 |
| *E230H-2013* | 1880–2150 | 0.1 × 0.09 | 4 | 6.05 | 423–3600 | 0.2 × 0.09 | 1 | 1.20 | 1200 |
| E230H-2063 | 1932–2205 | 0.1 × 0.09 | 1 | 0.35 | 352 | 0.1 × 0.09 | 1 | 1.53 | 1530 |
| E230H-2113 | 1976–2250 | 0.1 × 0.09 | 1 | 0.41 | 406 | 0.1 × 0.09 | 1 | 1.53 | 1530 |
| E230H-2163 | 2028–2296 | 0.1 × 0.09 | 1 | 0.36 | 363 | 0.1 × 0.09 | 1 | 1.53 | 1530 |
| E230H-2213 | 2077–2345 | 0.1 × 0.09 | 1 | 0.36 | 363 | 0.1 × 0.09 | 1 | 1.53 | 1530 |
| *E230H-2263* | 2135–2396 | 0.1 × 0.09 | 8 | 3.33 | 416 | 0.2 × 0.09 | 1 | 1.60 | 1600 |
| E230H-2313 | 2171–2441 | 0.1 × 0.09 | 3 | 1.98 | 423–1100 | 0.2 × 0.09 | 1 | 0.30 | 300 |
| E230H-2363 | 2227–2496 | 0.1, 0.2 × 0.09 | 3 | 0.95 | 229–382 | 0.2 × 0.09 | 1 | 1.10 | 1100 |
| E230H-2413 | 2274–2546 | 0.1 × 0.09 | 2 | 1.33 | 457–873 | 0.2 × 0.09 | 1 | 1.10 | 1100 |
| E230H-2463 | 2328–2606 | 0.1 × 0.09 | 2 | 1.02 | 512 | 0.1, 0.2 × 0.09 | 2 | 1.50 | 500–1000 |
| *E230H-2513* | 2379–2650 | 0.1 × 0.09 | 2 | 1.37 | 500–872 | 0.2 × 0.09 | 1 | 0.90 | 900 |
| E230H-2563 | 2431–2706 | 0.1 × 0.09 | 1 | 0.66 | 662 | 0.1, 0.2 × 0.09 | 2 | 1.40 | 250–1150 |
| E230H-2613 | 2486–2754 | 0.1 × 0.09 | 1 | 0.50 | 504 | 0.1 × 0.09 | 1 | 1.33 | 1325 |
| E230H-2663 | 2527–2804 | 0.1 × 0.09 | 2 | 1.31 | 564–743 | 0.2 × 0.09 | 1 | 1.10 | 1100 |
| E230H-2713 | 2578–2845 | 0.1 × 0.09 | 1 | 0.50 | 497 | 0.1 × 0.09 | 12 | 6.50 | 500–1000 |
| *E230H-2762* | 2621–2887 | 0.1 × 0.09 | 8 | 3.65 | 457 | 0.2 × 0.09 | 1 | 1.20 | 1200 |
| E230H-2812 | 2667–2942 | 0.1 × 0.09 | 2 | 0.99 | 490–503 | 0.1, 0.2 × 0.09 | 2 | 1.50 | 500–1000 |
| E230H-2862 | 2723–2999 | 0.1 × 0.09 | 2 | 1.21 | 476–732 | 0.2 × 0.09 | 1 | 1.10 | 1100 |
| E230H-2912 | 2772–3047 | … | … | … | … | 0.1 × 0.09 | 1 | 1.58 | 1580 |
| E230H-2962 | 2823–3095 | … | … | … | … | 0.1 × 0.09 | 1 | 1.58 | 1580 |
| *E230H-3012* | 2886–3159 | 0.1 × 0.09 | 2 | 5.20 | 1600–3600 | 0.2 × 0.09 | 1 | 1.20 | 1200 |

**Note.** Col. 1 is the STIS echelle setting (see description in Table 1 Notes): italicized are the prime CENWAVEs. Col. 2 is the approximate wavelength range of the setting post-SM4. (Note: the cited range can differ from the historical values in the STIS Exposure Time Calculator.) The next group of four columns is for the period 1997–2004; the second group of four is for 2009–present (post-SM4). Leading column of the first group, Col. 3, lists the aperture(s) used. Col. 4 is the number of exposures in that time range. Col. 5 is the total exposure. Col. 6 is the range of exposure durations for that group. Cols. 7–10 repeat 3–6 for the post-SM4 period.

in vacuum for both FUV and NUV. A Ritz wavelength in principle can be more accurate than a reported direct laboratory measurement of a specific transition, because the precision of the lower and upper energy-level assignments can benefit from wavelength measurements of all of the transitions that connect those levels to others, not only in the vacuum UV, but possibly also in the visible and near-infrared (where experimental wavelength standards, and measurement accuracy, can be much better).

An extensive collection of potential laboratory identifications was assembled from combined NIST lists of Pt I, Pt II, Ne II, Ne III, Cr I, and Cr II. Appendix A provides examples of

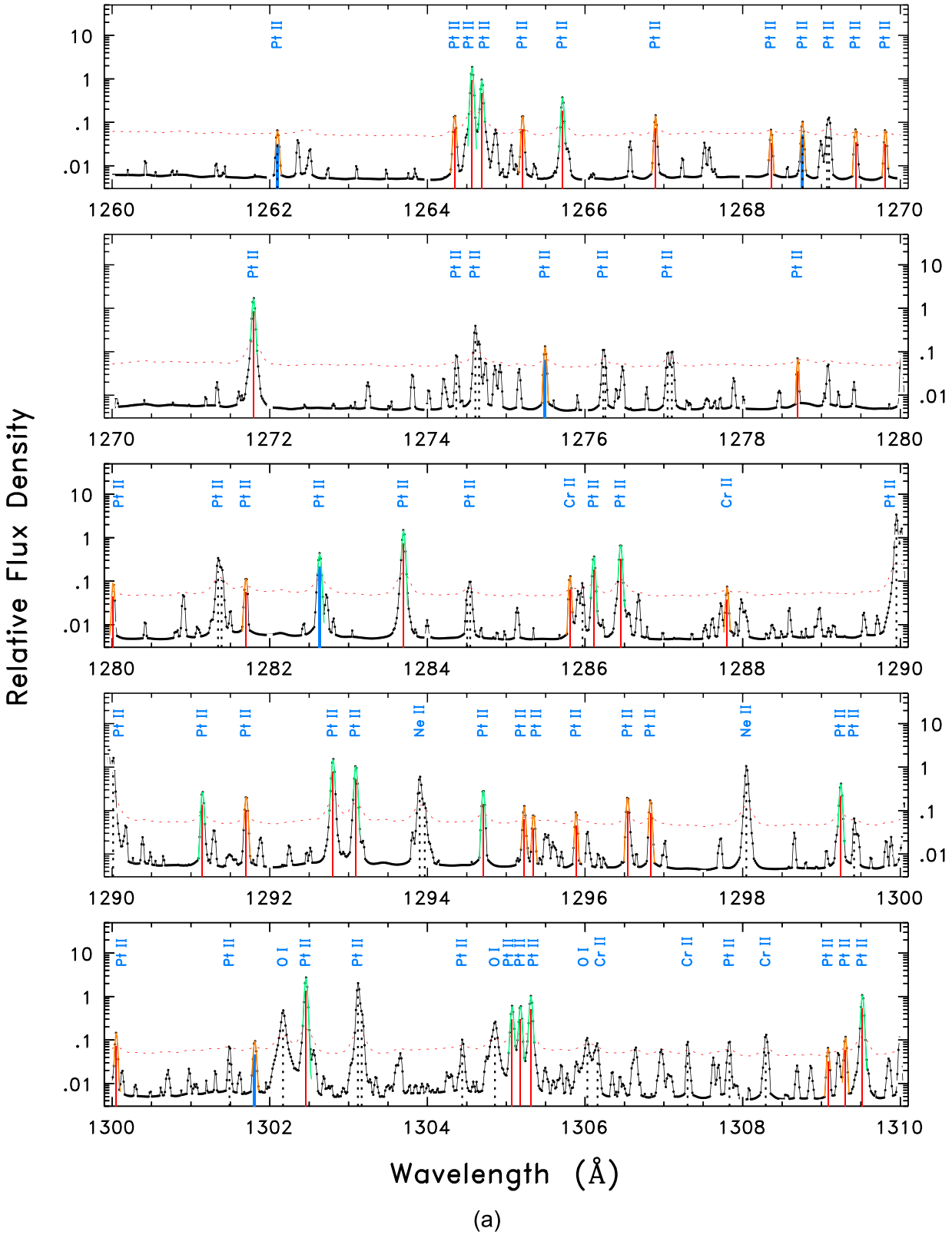


**Figure 2.** Examples of co-added STIS wavecal spectra. The lower intensity boundary is a heavily smoothed tracing of the $1\sigma$ photometric noise. A roughly horizontal, wavy dotted line represents a measurement threshold based on a multiple of the smoothed noise level. Identifications are provided for selected features. Vertical dotted lines indicate transitions that were rejected owing to close blends or other defects in the wavelengths. Solid vertical lines mark the emissions that were measured using a pseudo-Gaussian formalism. Red is for transitions with vetted laboratory wavelengths; blue (FUV only) are for empirically determined wavelengths (see text). The fitted profiles are depicted on top of the observed intensity points as smooth curves: green (S/N $>3\times$ the threshold) or orange (S/N $\leqslant 3\times$ the threshold). (a) A 50 Å section of E140M-1425, based on 25 wavecals totaling 17.9 ks of exposure. S/N threshold is $10\sigma$. (b) A 50 Å section of E230H-2713, based on 13 wavecals totaling 7.0 ks. S/N threshold is $7\sigma$.

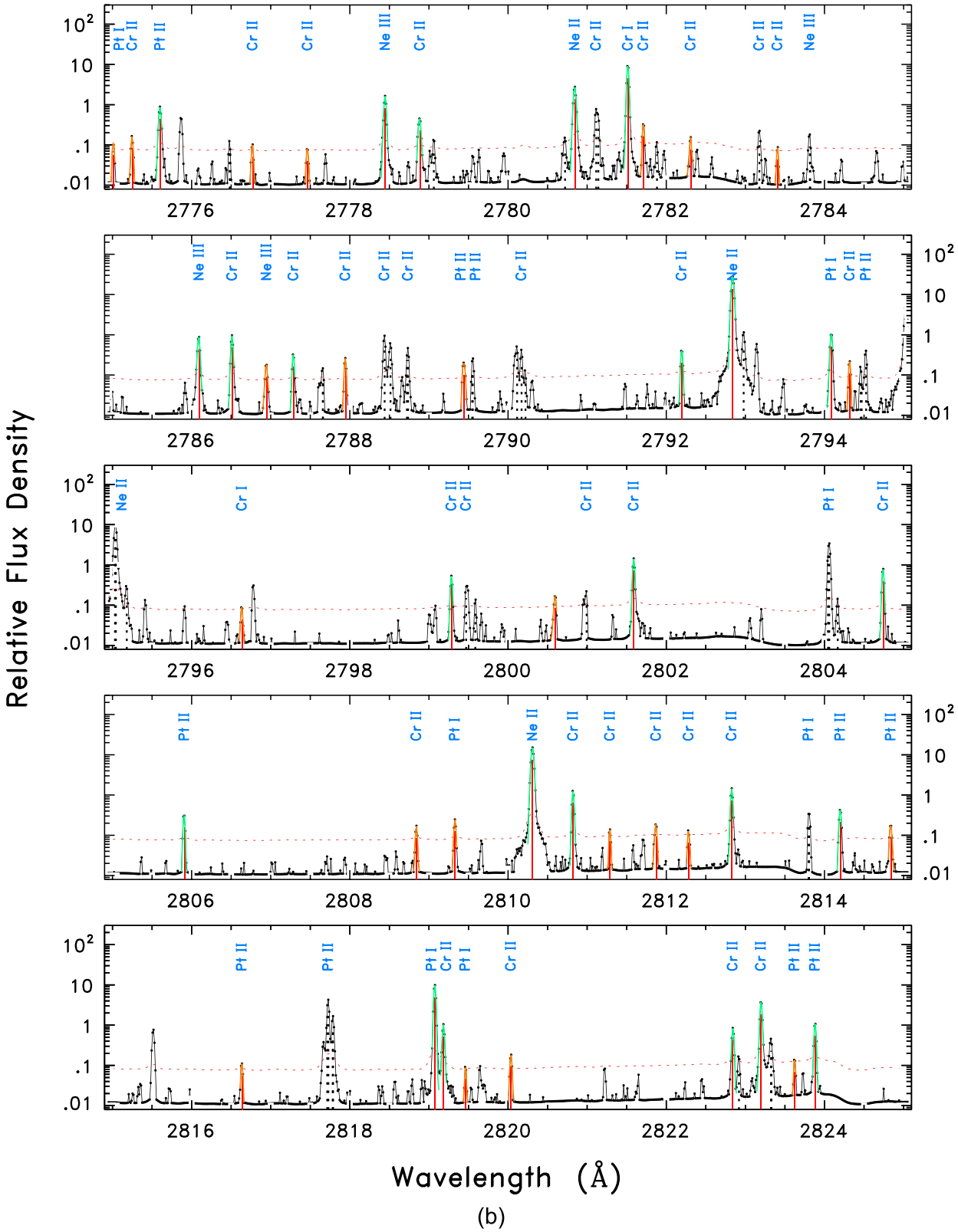


**Figure 2.** (Continued.)

the provenance of the NIST material. Possible identifications were examined carefully in spliced high-S/N FUV and NUV lamp spectra, obtained by concatenating all of the M-mode and H-mode spectra separately. Partially blended features, or poor quality laboratory wavelengths, could be identified straightforwardly and were eliminated from consideration. Occasionally, two, or more, different species might have transitions at essentially the same wavelength. Usually, but not always, it was possible to assign the feature uniquely to one of the species, based on excitation energy or strengths of other

members of the same multiplet. Ultimately, the success of the strategy rested on the ~69–440 (typically 190) lamp lines available for each CENWAVE, so that the final results were not sensitive to a few rogue wavelength assignments.

Solid vertical lines (mostly red but occasionally blue) mark the features that met the S/N criterion and ostensibly were single. These profiles were measured using the pseudo-Gaussian methodology, for reasons mentioned earlier. The wavelengths marked in blue, exclusively FUV, either were not present in the NIST tabulations, or the reported Ritz wavelength did not meet the 0.2 km $s^{-1}$ accuracy requirement. These wavelengths instead were derived empirically from a high-S/N splicing of all of the FUV high-resolution settings, corrected individually for the polynomial wavelength deviations (as described later), using CENWAVE-specific prototype models based solely on the accepted NIST lines. In essence, STIS was utilized as a laboratory spectrometer to measure the unidentified, or low-accuracy, transitions. This was done to increase the density of lines in the FUV, where the lamp spectrum is sparse, to help follow the long-range wavelength trends as precisely as possible, especially for E140M-1425 (the broad wavelength coverage of FUV-M required a higher-order polynomial compensation model than the more compact wavelength grasps of the H-resolution settings). Identifications for these empirically measured lines are from NIST, if the original wavelength failed the accuracy requirement, from other lists if not in NIST, or are blank if not in any of the existing tabulations. The fitted profiles are depicted on top of the observed intensity points as smooth curves: green for the highest S/N features; orange for moderate S/N.

Figures 3(a)–(c) illustrate the twelve STIS primary settings (one FUV-M, three FUV-H, two NUV-M, and six NUV-H), in groups of four. Each panel depicts wavelength residuals, expressed as equivalent velocities ($\Delta v = c(\lambda_{obs} - \lambda_{lab})/\lambda_{lab}$), as a function of wavelength across the grasp of the setting. The $y$-axis scales correspond roughly to $\pm 1$ resel. The smooth dashed curve is a polynomial fit of order 3, or higher in some cases. The faintly visible gray-scale image behind the points represents a probability density map constructed by numerous Monte Carlo trials refitting random realizations of the measured velocity shifts consistent with the assigned velocity errors. Widths of the distributions are roughly $\pm 1\sigma$. Yellow circled points are $\geqslant 3\sigma$ outliers excluded from the fit. The modeled long-range wavelength residuals are highly significant, yet the amplitudes typically are only a fraction of a resel, well within the original engineering specifications of the instrument. Nevertheless, the inherent wavelength precision of STIS clearly is much better than delivered by the relatively low-order polynomial dispersion relations utilized by the CALSTIS pipeline.

In general, the primary settings have greater calibration exposures than the less frequently used secondaries (the 32 of which are illustrated, in the same way as Figures 3, in Appendix B, Figure B1(a)–(h)), and display better dispersion fits for standard CALSTIS. Exceptions are: E140M-1425, which covers considerable spectral territory and has a pronounced negative velocity dip at the shortest wavelengths; E230M-1978, which also is wavelength extensive with a similar short-wavelength dip; E230H-1763, which has a smaller grasp, but again the short-wavelength dip; and E230H-2513, which shows a systematic positive offset in the middle of its range. A few cases, especially E230H-2762 (Figure 3(c)) and E230H-2812 (Figure B1(h)), appear to be afflicted by low-amplitude, high-frequency ripples. That could be the signature of a systematic velocity tilt on the scale of an echelle order, from one side of the order to the other. This effect can be seen in the corresponding panels of Figure 2 of Ayres (2010a: StarCAT), which depicts 2D distortion maps derived for the CALSTIS dispersion coefficients based on the wavecal material available from the initial STIS operations period (1997–2004). The panels for E230H-2762 and E230H-2812 clearly show the left–right asymmetry of the derived velocity maps. This issue cannot be solved by a 1D low-order polynomial correction (which is why $m$-resolved ASTRAL remains the standard). The amplitude of the wiggles is larger than the long-range changes in the wavelength direction—unlike neighboring CENWAVEs (e.g., E230H-2912; Figure B1(h)), which are dominated by the larger scale variation—but the standard deviation of the residuals still is only about a tenth of a resel.

Table 3 summarizes the polynomial fits illustrated in the previous Figure 3 (and B1(a)–(h)). The formulation is

$$\Delta v(\lambda) = C_0 + \sum_{i=1}^{n} C_i \left( \frac{(\lambda - \lambda_0)}{\Delta\lambda} \right)^i , \quad (1)$$

where $n$ is the polynomial degree, and the parameters $\lambda_0$ and $\Delta\lambda$ are unique to each CENWAVE. Here, $\Delta v$, in km $s^{-1}$, is the wavelength correction as a function of the pipeline-assigned $\lambda$ expressed in equivalent velocity units. The corrected wavelength, $\lambda_{corr}$, is:

$$\lambda_{corr} = \lambda - \frac{\Delta v(\lambda)}{c} \lambda , \quad (2)$$

where $c$ is the speed of light (in km $s^{-1}$). Notice in the table that most of the settings require just third order for the polynomial correction, nominally only one degree higher than the bi-quadratic formulation of the CALSTIS dispersion model.[11] Only a few cases—E140M-1425 and E140H-1307 in the FUV, and E230M-2124 in the NUV—required higher-order terms. That is a large improvement in simplicity compared to the complex $m$-resolved distortion maps implemented in the ASTRAL protocols. Most of the corrections are small—near the limits imposed by measurement errors and uncertainties in the fundamental laboratory wavelengths—except for a few of the CENWAVEs, which apparently have less than optimum CALSTIS dispersion coefficients.

The final diagrams, Figures 4(a)–(c), confront the proposed correction scheme with the previous ASTRAL version, applied to three representative post-SM4 settings, *using single-epoch exposures* to simplify the comparisons. Figure 4(a) is for FUV secondary setting E140H-1562 (ObsID obl601050; $t_{exp} = 2.6$ ks), Figure 4(b) is for NUV secondary E230H-1863 (ObsID oe1631010; 1.1 ks), and Figure 4(c) is for NUV primary setting E230H-2762 (ObsID oe1641010; 1.2 ks). Each figure shows, from top to bottom, the uncorrected standard CALSTIS merged x1d pipeline spectrum ("Cx"); the Cx spectrum corrected by the polynomial model from Table 3 ("Cz"); the merged x1d spectrum calibrated according to the ASTRAL dispersion relations ("Ax"); and the full ASTRAL protocols, namely the x1d file processed with the ASTRAL dispersion coefficients, further corrected with the $m$-resolved

[11] However, recall that $\lambda$ for a given echelle order $m$ and dispersion pixel $x$ is the solution of a quadratic equation, rather than the output of a simple polynomial.

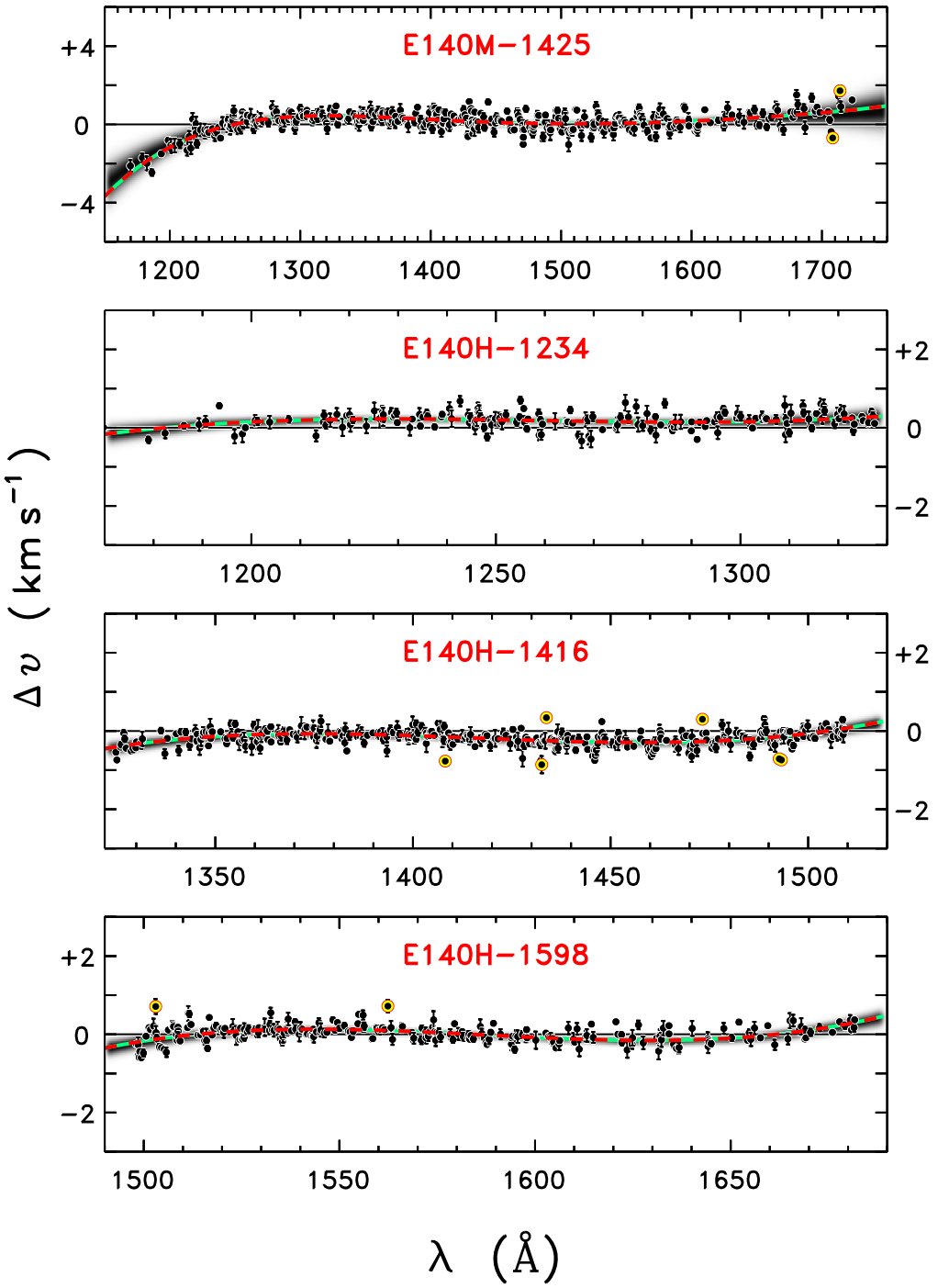


**Figure 3.** Wavelength residuals and fitted models for the twelve supported primary STIS echelle settings. Each panel depicts $\lambda_{obs} - \lambda_{lab}$, expressed as equivalent velocities, as a function of wavelength. The *y*-axis scales correspond roughly to $\pm 1$ resel. The smooth dashed curve is a polynomial of degree 3, or higher in some cases. The faintly visible gray-scale image behind the points is a probability density map representing uncertainties of the fit. Yellow circled dots are excluded $\geqslant 3\sigma$ outliers. (a) Single prime CENWAVE for FUV-M and the three for FUV-H; (b) the two prime CENWAVEs for NUV-M, and the leading two for NUV-H; (c) the final four NUV-H primes.

distortion map, then the echelle orders merged into a 1D spectrum ("Az"). In the two ASTRAL cases, an average zero-point shift was calculated and subtracted, as is done for routine science exposures under the ASTRAL protocols as determined from the companion auto-wavecal. The numerical values listed on the right-hand side of the panel headings are standard deviations of the velocity residuals with respect to the zero line (i.e., the laboratory reference frame).

The first example, Figure 4(a), is for the H-1562 CENWAVE. The top panel displays an asymmetric, roughly cubic trend of the velocity offsets, such that the wavelengths 1580–1620 Å are (blue)shifted by about $-1$ km s$^{-1}$ relative to the 1470–1510 Å interval. The average deviation is nearly zero and the standard deviation is 0.4 km s$^{-1}$. The next panel down illustrates the corrected spectrum, now flattened, with a $\sim 2\times$ smaller $\sigma$ with respect to the zero line. The panel second from the bottom, Ax,

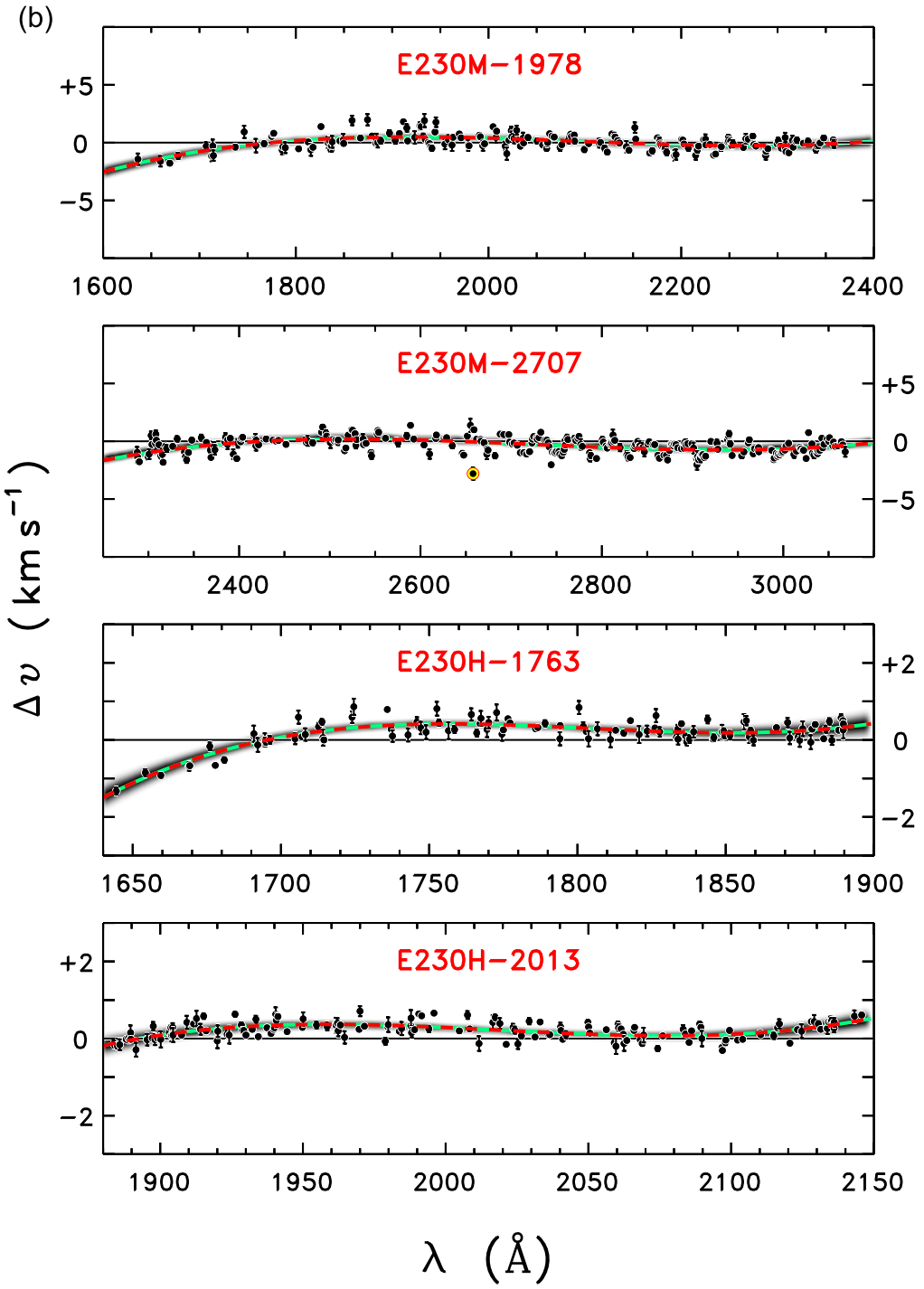


**Figure 3.** (Continued.)

shows the result of the pipeline processing with the ASTRAL dispersion relations (and other key reference files), but no further correction (aside from the zero-point shift). The cubic wave still is present, but is more symmetric and reduced in amplitude relative to standard CALSTIS, with a similar $\sigma$ to that of *corrected* standard CALSTIS. The reduced $\sigma$ demonstrates the value of implementing upgraded dispersion reference files, even without any further corrections. The lowest panel shows the result of applying the ASTRAL distortion correction to the processed x1d file, then merging the orders. The velocity residuals are somewhat flattened compared with the uncorrected distribution, but show essentially the same $\sigma$. This is an example where the ASTRAL model was less well defined: the previously available (pre-2016) wavecals for that CENWAVE were only about 2.9 ks in total duration, compared with the $t_{\rm tot} \gtrsim 10$ ks typical of the E140H primary settings.

The second example, Figure 4(b), is for NUV secondary setting H-1863. The comparison is similar in some respects to previous Figure 4(a), although there were fewer high-S/N lines that could be measured, partly owing to the enhanced backgrounds, and associated elevated noise levels, of the NUV channel post-SM4. The standard CALSTIS dispersion coefficients produce a strong

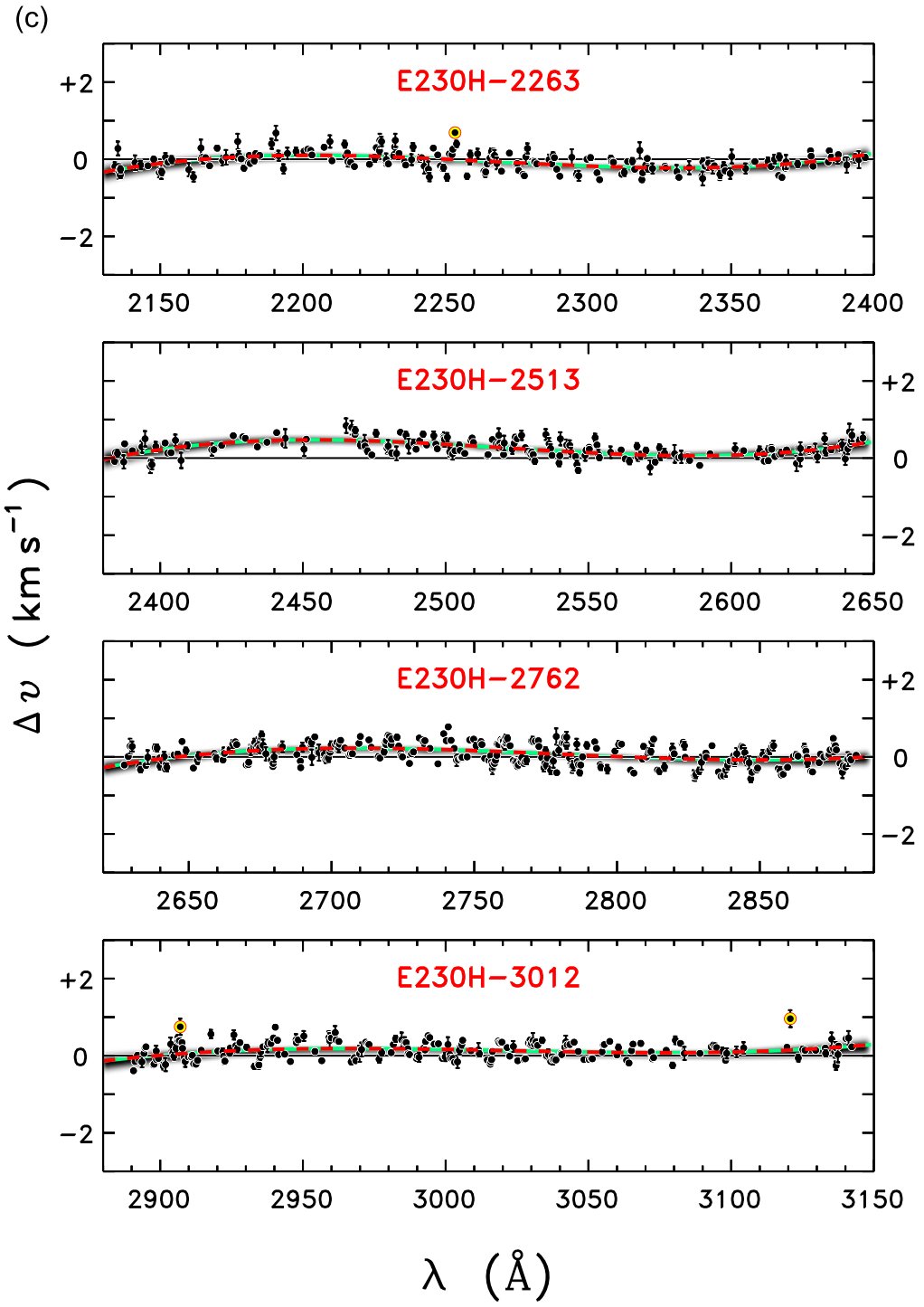


**Figure 3.** (Continued.)

cubic wave in the uncorrected spectrum, now with a significant positive zero-point offset and again a large standard deviation. The spectrum is flattened when the polynomial correction is applied to the merged x1d tracing, again reducing the $\sigma$, now by a factor of three (partly due to the compensation for the large systematic offset of the Cx version). In the Ax panel, like previous Figure 4(a), the new ASTRAL dispersion relations produce a more symmetric, lower amplitude cubic wave, with a $\sigma$ only somewhat larger than for the corrected standard CALSTIS. The 2D ASTRAL correction further flattens the spectrum, noticeably reducing the $\sigma$.

The third example, Figure 4(c), is for primary setting H-2762. The major difference with respect to the previous comparisons is that the standard CALSTIS dispersion coefficients produce only a barely noticeable wave in the uncorrected spectrum, although there are apparent high-frequency oscillations at the long-wavelength end of the setting (alluded to previously). The spectrum once again is flattened when the polynomial correction is applied to the merged x1d tracing, although the dispersion in velocity residuals was muted only slightly. In the Ax panel, the ASTRAL dispersion relations produce essentially the same outcome as corrected standard

**Table 3**
STIS Wavelength Correction Polynomials

| Setting | $\lambda_0$ | $\Delta\lambda$ | $n$ | $\chi^2$ | $\sigma_c$ [$\sigma_u$] |
|---|---|---|---|---|---|
| | (Å) | | | | (km s$^{-1}$) |
| $C_0 \pm \sigma_0$ | $C_1 \pm \sigma_1$ | $C_2 \pm \sigma_2$ | $C_3 \pm \sigma_3$ | $C_4 \pm \sigma_4$ | $C_5 \pm \sigma_5$ |
| (1) | (2) | (3) | (4) | (5) | (6) |
| | | | FUV-M | | |
| *E140M-1425* | 1450.0 | 280.0 | 5 | 3.2 | 0.36 [0.52] |
| +0.103 ± 0.015 | −0.647 ± 0.071 | +1.302 ± 0.131 | +1.149 ± 0.346 | −2.249 ± 0.180 | +1.129 ± 0.361 |
| | | | FUV-H | | |
| *E140H-1234* | 1250.0 | 80.0 | 3 | 1.1 | 0.20 [0.28] |
| +0.200 ± 0.020 | −0.144 ± 0.064 | −0.132 ± 0.060 | +0.379 ± 0.107 | | |
| E140H-1271 | 1262.5 | 92.5 | 3 | 1.2 | 0.19 [0.25] |
| +0.170 ± 0.015 | −0.201 ± 0.047 | −0.475 ± 0.046 | +0.727 ± 0.082 | | |
| E140H-1307 | 1300.0 | 95.0 | 4 | 1.2 | 0.19 [0.34] |
| +0.190 ± 0.022 | −0.406 ± 0.049 | +0.624 ± 0.132 | +0.720 ± 0.080 | −0.883 ± 0.152 | |
| E140H-1343 | 1342.5 | 97.5 | 3 | 1.1 | 0.17 [0.28] |
| +0.028 ± 0.015 | −0.639 ± 0.045 | +0.217 ± 0.035 | +0.609 ± 0.069 | | |
| E140H-1380 | 1377.5 | 97.5 | 3 | 1.4 | 0.20 [0.37] |
| −0.002 ± 0.016 | −0.797 ± 0.048 | +0.152 ± 0.039 | +0.450 ± 0.079 | | |
| *E140H-1416* | 1417.5 | 92.5 | 3 | 1.1 | 0.17 [0.27] |
| −0.187 ± 0.013 | −0.373 ± 0.039 | +0.025 ± 0.031 | +0.616 ± 0.060 | | |
| E140H-1453 | 1457.5 | 92.5 | 3 | 1.6 | 0.23 [0.33] |
| −0.142 ± 0.023 | −0.662 ± 0.069 | −0.065 ± 0.061 | +0.762 ± 0.108 | | |
| E140H-1489 | 1487.5 | 97.5 | 3 | 1.8 | 0.21 [0.55] |
| +0.287 ± 0.015 | −0.955 ± 0.045 | +0.139 ± 0.038 | +0.701 ± 0.074 | | |
| E140H-1526 | 1522.5 | 97.5 | 3 | 1.4 | 0.19 [0.45] |
| +0.016 ± 0.017 | −0.968 ± 0.050 | +0.114 ± 0.046 | +0.557 ± 0.085 | | |
| E140H-1562 | 1560.0 | 95.0 | 3 | 1.2 | 0.18 [0.34] |
| −0.301 ± 0.019 | −0.926 ± 0.056 | +0.312 ± 0.052 | +0.803 ± 0.094 | | |
| *E140H-1598* | 1590.0 | 95.0 | 3 | 1.1 | 0.18 [0.21] |
| −0.031 ± 0.017 | −0.476 ± 0.051 | +0.087 ± 0.040 | +0.789 ± 0.079 | | |
| | | | NUV-M | | |
| *E230M-1978* | 1995.0 | 365.0 | 3 | 5.1 | 0.55 [0.66] |
| +0.406 ± 0.025 | −0.793 ± 0.075 | −1.404 ± 0.090 | +1.704 ± 0.145 | | |
| E230M-2124 | 2130.0 | 390.0 | 4 | 7.8 | 0.65 [0.93] |
| +0.898 ± 0.037 | −1.740 ± 0.089 | −4.754 ± 0.252 | +2.676 ± 0.152 | +3.567 ± 0.299 | |
| E230M-2269 | 2270.0 | 390.0 | 3 | 5.2 | 0.55 [0.84] |
| −0.628 ± 0.024 | −1.119 ± 0.075 | +0.376 ± 0.060 | +1.987 ± 0.118 | | |
| E230M-2415 | 2390.0 | 390.0 | 3 | 10.5 | 0.70 [1.24] |
| +0.867 ± 0.024 | −2.164 ± 0.073 | −0.267 ± 0.056 | +1.127 ± 0.112 | | |
| E230M-2561 | 2550.0 | 380.0 | 3 | 15.8 | 0.73 [1.50] |
| +0.516 ± 0.020 | −2.501 ± 0.052 | −0.258 ± 0.043 | +1.266 ± 0.079 | | |
| *E230M-2707* | 2680.0 | 390.0 | 3 | 9.0 | 0.59 [0.79] |
| −0.114 ± 0.018 | −1.271 ± 0.050 | −0.610 ± 0.037 | +1.645 ± 0.072 | | |
| | | | NUV-H | | |
| *E230H-1763* | 1765.0 | 125.0 | 3 | 1.1 | 0.20 [0.43] |
| +0.410 ± 0.027 | −0.148 ± 0.075 | −0.992 ± 0.062 | +1.060 ± 0.109 | | |
| E230H-1813 | 1820.0 | 130.0 | 3 | 0.9 | 0.19 [0.46] |
| +0.562 ± 0.024 | −0.513 ± 0.065 | −0.468 ± 0.053 | +0.899 ± 0.099 | | |
| E230H-1863 | 1865.0 | 130.0 | 3 | 0.8 | 0.16 [0.84] |
| +0.859 ± 0.033 | −1.273 ± 0.085 | −0.114 ± 0.072 | +0.988 ± 0.125 | | |
| E230H-1913 | 1917.5 | 132.5 | 3 | 1.0 | 0.16 [0.58] |
| +0.343 ± 0.024 | −1.286 ± 0.078 | +0.139 ± 0.059 | +1.101 ± 0.120 | | |
| E230H-1963 | 1972.5 | 127.5 | 3 | 1.1 | 0.16 [0.41] |
| −0.023 ± 0.027 | −1.040 ± 0.072 | +0.103 ± 0.060 | +0.680 ± 0.107 | | |
| *E230H-2013* | 2015.0 | 130.0 | 3 | 1.1 | 0.18 [0.30] |
| +0.233 ± 0.022 | −0.481 ± 0.059 | −0.053 ± 0.045 | +0.766 ± 0.087 | | |

**Table 3**
(Continued)

| Setting | $\lambda_0$ (Å) | $\Delta\lambda$ | $n$ | $\chi^2$ | $\sigma_c$ [$\sigma_u$] (km s$^{-1}$) |
|---|---|---|---|---|---|
| $C_0 \pm \sigma_0$ (1) | $C_1 \pm \sigma_1$ (2) | $C_2 \pm \sigma_2$ (3) | $C_3 \pm \sigma_3$ (4) | $C_4 \pm \sigma_4$ (5) | $C_5 \pm \sigma_5$ (6) |
| E230H-2063 | 2072.5 | 132.5 | 3 | 1.2 | 0.17 [0.47] |
| +0.332 ± 0.029 | −1.036 ± 0.098 | −0.104 ± 0.070 | +0.770 ± 0.149 | | |
| E230H-2113 | 2120.0 | 135.0 | 3 | 1.1 | 0.19 [0.40] |
| +0.033 ± 0.028 | −1.084 ± 0.078 | −0.048 ± 0.065 | +0.911 ± 0.119 | | |
| E230H-2163 | 2162.5 | 127.5 | 3 | 0.9 | 0.15 [0.45] |
| −0.056 ± 0.029 | −1.010 ± 0.077 | −0.226 ± 0.060 | +0.664 ± 0.113 | | |
| E230H-2213 | 2215.0 | 130.0 | 3 | 0.9 | 0.17 [0.44] |
| −0.259 ± 0.027 | −0.969 ± 0.082 | −0.040 ± 0.062 | +0.852 ± 0.123 | | |
| *E230H-2263* | 2267.5 | 132.5 | 3 | 1.3 | 0.20 [0.24] |
| −0.064 ± 0.018 | −0.506 ± 0.054 | +0.006 ± 0.043 | +0.718 ± 0.085 | | |
| E230H-2313 | 2310.0 | 130.0 | 3 | 1.4 | 0.19 [0.30] |
| −0.246 ± 0.022 | −0.537 ± 0.063 | +0.168 ± 0.049 | +0.821 ± 0.091 | | |
| E230H-2363 | 2362.5 | 132.5 | 3 | 1.3 | 0.19 [0.42] |
| +0.117 ± 0.022 | −0.991 ± 0.065 | +0.005 ± 0.047 | +0.790 ± 0.097 | | |
| E230H-2413 | 2410.0 | 135.0 | 3 | 0.9 | 0.17 [0.26] |
| −0.021 ± 0.023 | −0.770 ± 0.063 | +0.093 ± 0.048 | +0.873 ± 0.098 | | |
| E230H-2463 | 2465.0 | 125.0 | 3 | 0.9 | 0.16 [0.21] |
| +0.092 ± 0.024 | −0.525 ± 0.063 | −0.133 ± 0.053 | +0.605 ± 0.096 | | |
| *E230H-2513* | 2517.5 | 132.5 | 3 | 1.0 | 0.18 [0.34] |
| +0.278 ± 0.018 | −0.610 ± 0.063 | −0.046 ± 0.041 | +0.808 ± 0.091 | | |
| E230H-2563 | 2565.0 | 125.0 | 3 | 1.3 | 0.19 [0.27] |
| −0.125 ± 0.022 | −0.581 ± 0.058 | +0.144 ± 0.050 | +0.453 ± 0.089 | | |
| E230H-2613 | 2617.5 | 127.5 | 3 | 1.0 | 0.16 [0.34] |
| +0.151 ± 0.023 | −0.823 ± 0.063 | −0.034 ± 0.046 | +0.635 ± 0.095 | | |
| E230H-2663 | 2660.0 | 130.0 | 3 | 0.9 | 0.17 [0.24] |
| +0.085 ± 0.018 | −0.602 ± 0.053 | −0.022 ± 0.038 | +0.548 ± 0.080 | | |
| E230H-2713 | 2707.5 | 122.5 | 3 | 0.9 | 0.15 [0.29] |
| −0.176 ± 0.016 | −0.561 ± 0.045 | +0.012 ± 0.039 | +0.644 ± 0.071 | | |
| *E230H-2762* | 2755.0 | 130.0 | 3 | 2.3 | 0.25 [0.28] |
| +0.149 ± 0.014 | −0.374 ± 0.043 | −0.262 ± 0.032 | +0.475 ± 0.067 | | |
| E230H-2812 | 2800.0 | 130.0 | 3 | 2.0 | 0.24 [0.28] |
| +0.134 ± 0.016 | −0.357 ± 0.044 | −0.204 ± 0.038 | +0.498 ± 0.070 | | |
| E230H-2862 | 2855.0 | 130.0 | 3 | 0.9 | 0.16 [0.22] |
| +0.033 ± 0.016 | −0.501 ± 0.048 | −0.261 ± 0.040 | +0.493 ± 0.080 | | |
| E230H-2912 | 2910.0 | 135.0 | 3 | 0.9 | 0.15 [0.32] |
| +0.088 ± 0.020 | −0.798 ± 0.057 | −0.005 ± 0.043 | +0.594 ± 0.087 | | |
| E230H-2962 | 2962.5 | 127.5 | 3 | 0.9 | 0.16 [0.25] |
| +0.089 ± 0.021 | −0.627 ± 0.052 | −0.120 ± 0.051 | +0.614 ± 0.088 | | |
| *E230H-3012* | 3017.5 | 127.5 | 3 | 1.7 | 0.21 [0.26] |
| +0.140 ± 0.015 | −0.192 ± 0.052 | −0.037 ± 0.038 | +0.352 ± 0.076 | | |

**Note.** There are alternating rows. In the first row of each pair, Col. 1 lists a STIS echelle setting. The primary CENWAVEs are italicized. Cols. 2 and 3 are parameters that define the independent variable in the polynomial model. Col. 4 is the polynomial degree. Col. 5 is the (reduced) $\chi^2$ of the fit. The leading value in Col. 6, $\sigma_c$, is the standard deviation of the measured wavelength offsets with respect to the fit, expressed in equivalent velocity units. The trailing bracketed value, $\sigma_u$, is the equivalent standard deviation of the initial, uncorrected fluxes relative to the zero line (i.e., the laboratory frame). The columns in the second row of each pair list the $n + 1$ coefficients, $C_i$, of the polynomial model (see Equation (1) in the text).

CALSTIS (a theme repeated for many of the primary settings possessing adequate pre-flight calibrations). The additional ASTRAL distortion correction again somewhat flattens the spectrum, reducing the $\sigma$ modestly. The fact that the circa 2016 ASTRAL dispersion relations yield about the same $\sigma$ as corrected standard CALSTIS suggests that the conspicuous rippling of the spectrum cannot be removed simply through the dispersion model, but rather has a higher-order aspect that can be treated most successfully by a more complex scheme like the $m$-dependent ASTRAL distortion maps.

The large systematic offsets noted above for some of the more poorly calibrated secondary settings could be a concern in studies that require high-precision wavelengths. The proposed polynomial correction can compensate for the major influence of

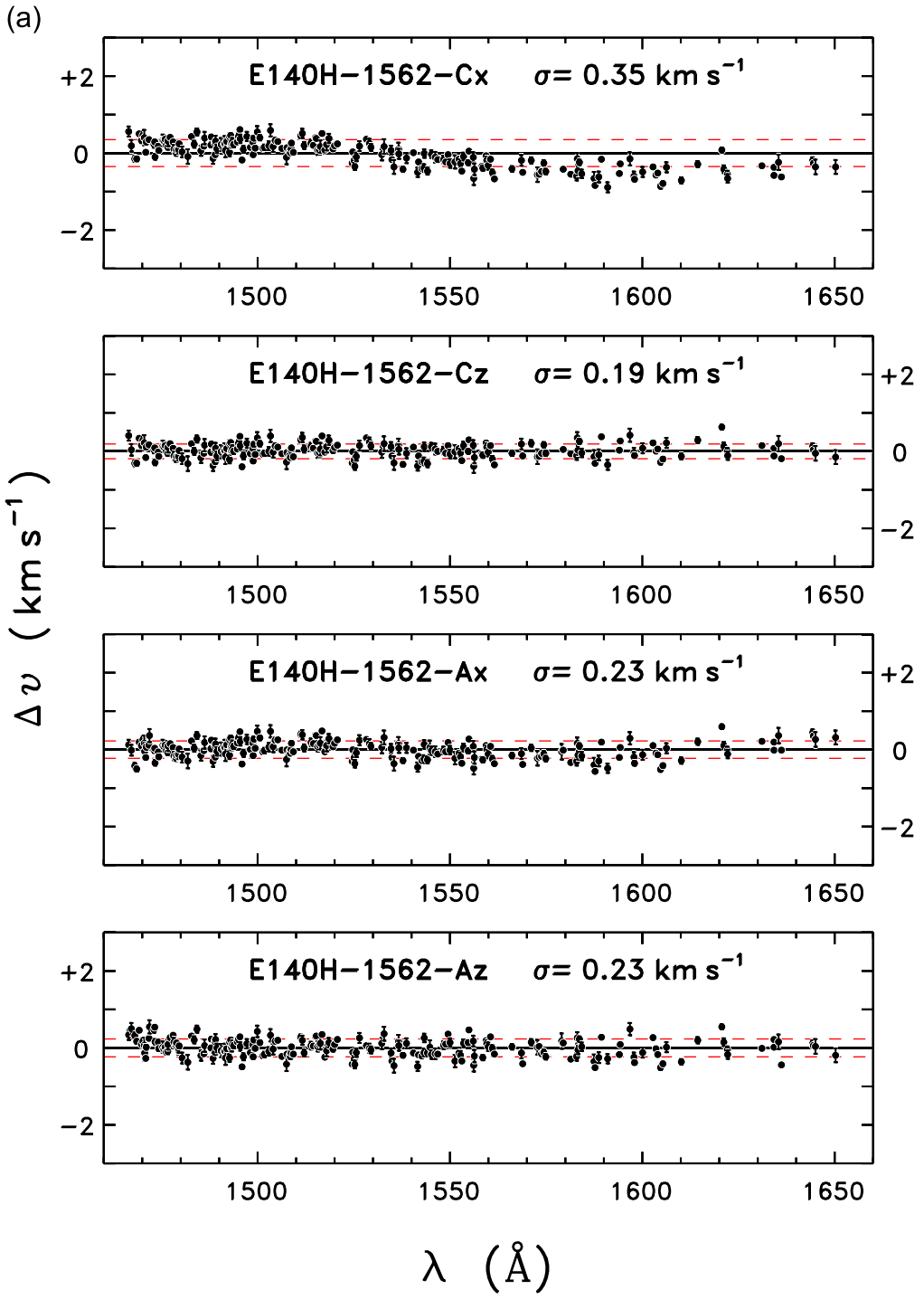


**Figure 4.** Wavelength residuals, in equivalent velocities. "Cx" (top panel) refers to standard CALSTIS; "Cz" (second from top) is Cx corrected during post-processing with a third-order polynomial in $\lambda$; "Ax" (second from bottom) denotes processing by CALSTIS with ASTRAL reference files, including updated dispersion coefficients; and "Az" (bottom panel) is Ax corrected post-facto by an ASTRAL distortion map. Numerical values in the titles are the standard deviations of the residuals around the zero line, illustrated by horizontal red dashed lines ($\pm 1\sigma$) in the individual panels. These comparisons are for single wavecal exposures, rather than the co-added spectra of Figures 3, thus the standard deviations for the Cx cases can differ from the bracketed values in Table 3. The secondary settings are noted in a dark font; the one primary is in red. (a) FUV secondary setting E140H-1562; (b) NUV secondary setting E230H-1863; (c) NUV primary setting E230H-2762.

such dispersion offsets. Nevertheless, some uncertainty can be introduced by the auto-wavecal associated with a science observation, which is utilized internally by CALSTIS to compensate for small thermally driven global wavelength shifts. Uncertainties in the wavecal offset is of minimal concern for the normal ASTRAL science processing, because, as alluded to earlier, the target data set and the companion short-exposure auto-wavecal both are processed through CALSTIS and the post-facto distortion correction protocol in exactly the same way. Any significant displacement of the processed auto-wavecal, deduced from the average shifts of high-S/N lamp lines, then is applied as a global velocity correction to the target spectrum. At the same time, the Pt/Ne-Cr lamps have slowly been fading in brightness over time, but the default wavecal exposure times

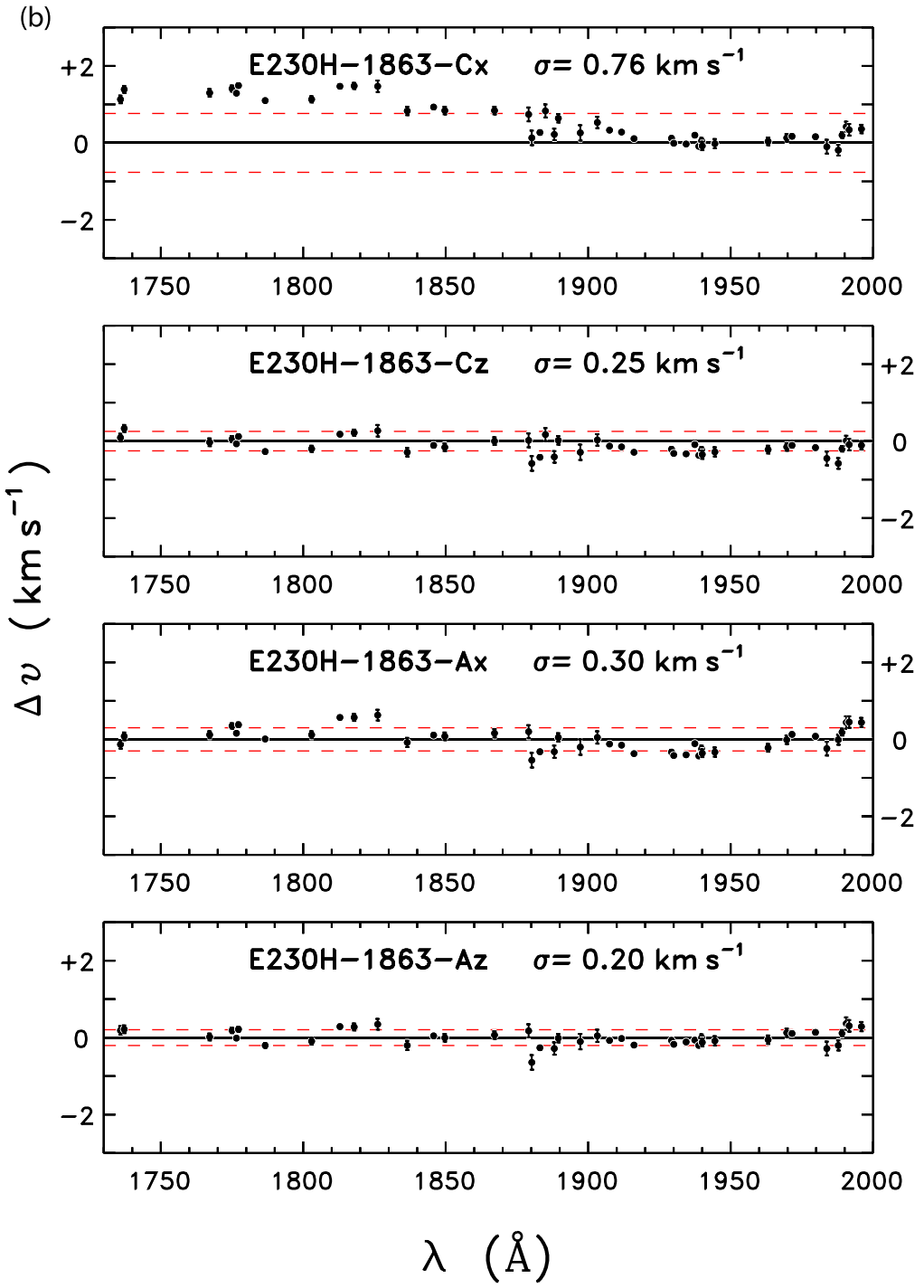


**Figure 4.** (Continued.)

have remained the same. Often, especially for the short-wavelength FUV-H CENWAVEs, there might be only one or two bright-enough emission spots in the raw auto-wavecal to allow a successful CALSTIS cross-correlation (or the post-facto ASTRAL correction), so the accuracy rests on the precision of essentially only a single line (rather than on a statistically robust ensemble of such features, as in the more general case). For that reason, it has become common practice in the past few years for FUV programs that require accurate wavelengths to insert nonstandard, deeper lamp exposures in their observing scripts.

## 4. Summary

This study focused on subtle wavelength distortions in STIS UV echelle spectra, which are not fully corrected by the low-order dispersion model in the CALSTIS pipeline. Most STIS investigators would find the standard pipeline files to be completely adequate in terms of wavelength precision, but those who press the instrumental limits could benefit from a correction scheme (or, at least be aware that the underlying deviations exist). The dominant shape of the residual wavelength distortion is a cubic polynomial, so comparisons

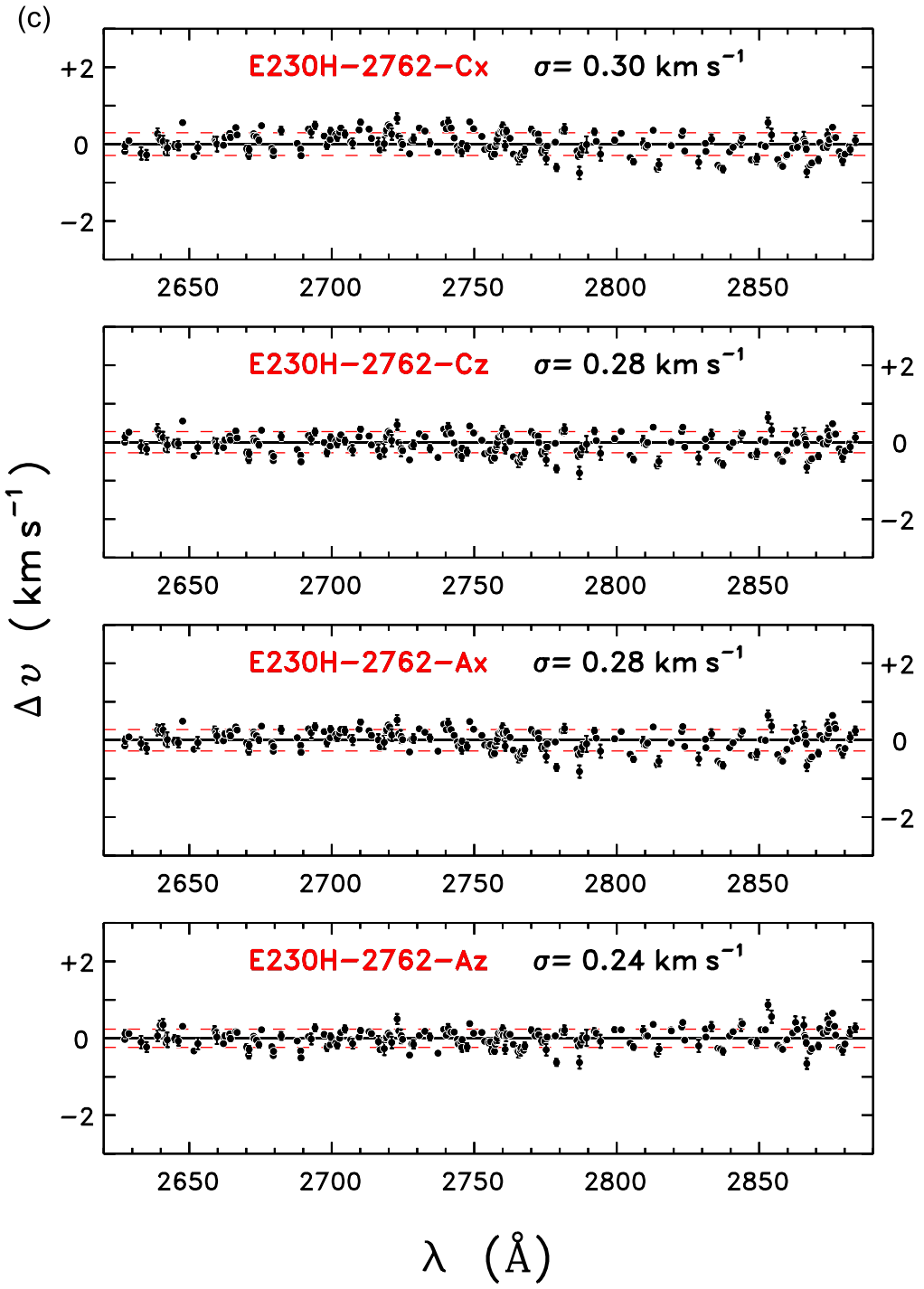


**Figure 4.** (Continued.)

of emission line velocities at the short end of a CENWAVE to those at the long end could experience maximum relative errors, which might be important in certain investigations.

Two main takeaways of the study:

1. New dispersion coefficients, based on the best available wavecal material and laboratory line lists, can improve the precision of the STIS wavelength scales, even without any post-facto corrections.
2. Additional suppression of residual velocity errors can be accomplished by a straightforward low-order polynomial correction applied to the merged pipeline x1d file. Although the polynomial model only is a partial solution to the wavelength correction conundrum, the improvements can approach those of full ($m$, $\lambda$) schemes.

Further, there might be straightforward modifications to the CALSTIS dispersion polynomials that could accomplish much of the spectral flattening even without a post-facto correction. Schematic experimentation (Ayres 2010b: "Ironing out the Wrinkles in STIS") found that adding a few extra, higher-order terms to the CALSTIS dispersion formula could improve the

wavelength precision for many of the echelle CENWAVEs, although unfortunately not so much for the heavily used E140M-1425 setting.

The standard CALSTIS formulation has a fundamental limitation, however. As mentioned earlier, the model relates the $x$ (dispersion direction) pixel position to a second-order polynomial in various combinations of $m$ and $\lambda$, $x = f(m, \lambda)$. Thus, in effect, the wavelength assignments are the result of solving a quadratic equation in $\lambda$, given a fixed $m$. However, the dominant wavelength correction demonstrated here, expressed in equivalent velocities (proportional to $\Delta\lambda/\lambda$), is a cubic polynomial in $\lambda$, which would be fourth order for $\Delta\lambda$ by itself. Consequently, replacing $\lambda$ with, say, $\lambda - \Delta\lambda$, in the standard dispersion model would generate terms up to $n = 8$ in $\lambda$, which would be unwieldy at best; but even more complex for the (few, though important) CENWAVEs that required fourth- or fifth-order corrections in $\Delta v$. A way around this complexity might be to recast the dispersion model as $\lambda = f(m, x) + \Delta\lambda$, and iteratively solve for the correction term to yield a final $\lambda$ for each pixel. However, the implementation would require major surgery on CALSTIS, so for the moment the post-facto correction schemes seem most practical.

In the end, repopulating CALSTIS dispersion coefficients for all of the STIS echelle settings would be an important step toward modernizing the pipeline. In fact, the current dispersion reference files for the FUV and NUV echelles are based on pre-flight data (i.e., prior to 1997), and apparently have not been updated since. Meanwhile, NIST investigators, and others, have made dedicated efforts to improve and expand the fundamental Pt, Ne, and Cr line lists based on detailed measurements of STIS flight-lamp spares (e.g., Sansonetti et al. 2004; Sansonetti & Nave 2014; also Appendix A). Further, the routine wavelength calibration programs of the STIS team, supplemented by Guest Observer efforts, have collected a full set of post-SM4 deep wavecal exposures on orbit for all of the CENWAVEs. Now, a quarter century into the STIS era, is an opportune time to upgrade the CALSTIS pipeline, for the sake of retrospective, contemporary, and future investigations with the premier high-resolution UV spectrograph in space.

I thank Daniel Welty and Charles Proffitt of the Space Telescope Science Institute (STScI) for their valuable input at several stages of this study. This work was supported by grant HST-GO-15948.001-A from STScI, based on observations from Hubble Space Telescope collected at STScI, operated by the Associated Universities for Research in Astronomy, under contract to NASA. This investigation made extensive use of the Atomic Spectra Database hosted by the National Institute of Standards and Technology, Gaithersburg, Maryland. HST/STIS wavelength calibration spectra were obtained from the Mikulski Archive for Space Telescopes (MAST) at STScI in Baltimore, Maryland. The specific data sets can be accessed via 10.17909/t9-4hrc-wz73.

## Appendix A
## Examples of NIST Atomic Physics Data Available for the STIS Wavecal Lamps

The following are selected references from NIST relevant to the wavelengths and energy levels of spectral emissions from the STIS Pt/Ne-Cr calibration lamps.

### *A.1. General*

"Characterization of the Far-Ultraviolet Spectrum of Pt/Cr-Ne Hollow Cathode Lamps as Used on the Space Telescope Imaging Spectrograph on Board the Hubble Space Telescope," C. J. Sansonetti, F. Kerber, J. Reader, & M. R. Rosa, *Astrophys. J., Suppl. Ser.* 153, 555–579 (2004) DOI:10.1086/421874.

"Spectral Characterization of HST Calibration Lamps: New Pt/Cr-Ne Line Catalogues and Ageing Test," F. Kerber, M. R. Rosa, C. J. Sansonetti, J. Reader, G. Nave, P. Bristow, M. Fiorentino, & G. Lercher, in *UV and Gamma Ray Space Telescope Systems, Proc. SPIE 5488*, 679–690 (edited by G. Hasinger & M. J. L. Turner, 2004) DOI:10.1117/12.550507.

### *A.2. Pt I and Pt II*

Most of the modern Pt I and Pt II laboratory measurements are described in the references under the preceding "General" heading.

"Reference Wavelengths in the Spectra of Fe, Ge, and Pt in the Region Near 1935 Å," G. Nave and C. J. Sansonetti, *J. Opt. Soc. Am. B* 21, 442–453 (2004) DOI:10.1364/JOSAB.21.000442.

### *A.3. Ne II and Ne III*

"The Ne II Spectrum," A. E. Kramida & G. Nave, *Eur. Phys. J. D* 39, 331–350 (2006) DOI:10.1140/epjd/e2006-00121-4.

"New FTS Measurements, Optimized Energy Levels and Refined VUV Standards in the Ne III Spectrum," A. E. Kramida & G. Nave, *Eur. Phys. J. D* 37, 1–21 (2006) DOI:10.1140/epjd/e2005-00249-7.

### *A.4. Cr I and Cr II*

"Extended Analysis of the Spectrum of Singly Ionized Chromium (Cr II)," C. J. Sansonetti & G. Nave, *Astrophys. J., Suppl. Ser.* 213, 28 (2014) DOI:10.1088/0067-0049/213/2/28.

"Comprehensive Observations of the Ultraviolet Spectrum and Improved Energy Levels for Singly Ionized Chromium (Cr II)," C. J. Sansonetti, G. Nave, J. Reader, & F. Kerber, *Astrophys. J., Suppl. Ser.* 202, 15 (2012) DOI:10.1088/0067-0049/202/2/15.

"Energy Levels and Observed Spectral Lines of Neutral and Singly Ionized Chromium, Cr I and Cr II," E. B. Saloman, *J. Phys. Chem. Ref. Data* 41, 043103 (2012) DOI:10.1063/1.4754694.

"The 236.6-5400.0 nm Spectrum of Cr I," L. Wallace & K. Hinkle, *Astrophys. J.* 700, 720–726 (2009) DOI:10.1088/0004-637X/700/1/720.

## Appendix B
## Supplementary Figures for the STIS Secondary Echelle Settings

Figures 3(a)–(c) previously illustrated velocity residuals and correction polynomials for the 12 primary echelle CENWAVEs of STIS. As was noted then, the primary settings in most cases have better-defined dispersion coefficients than the more numerous, but less frequently used and less well calibrated, secondary CENWAVEs. The following Figures B1(a)–(h) present similar comparisons as Figures 3 for the 32

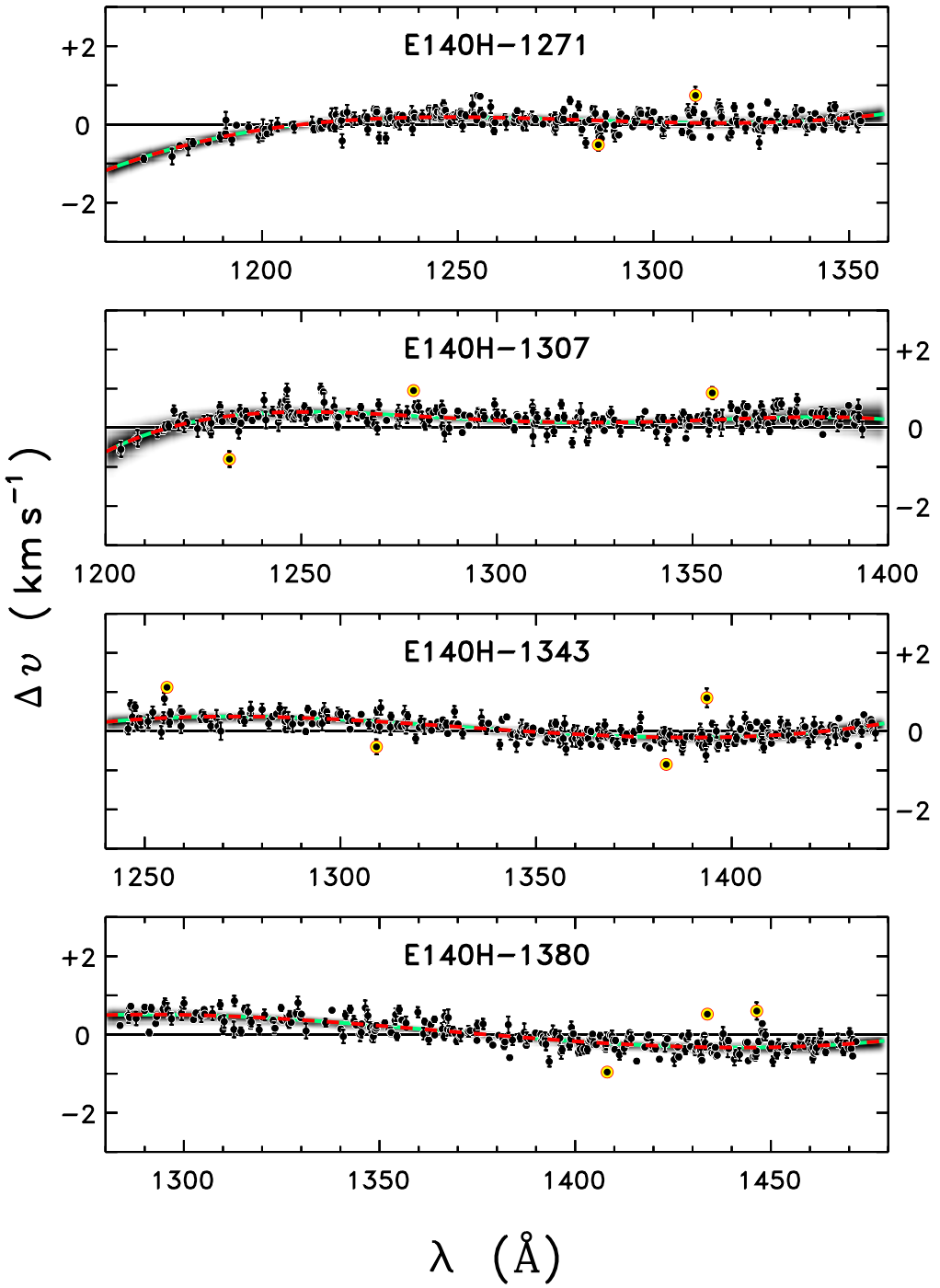


**Figure B1.** Similar to Figures 3(a)–(c) for the secondary echelle settings (indicated by panel titles in a dark font).
(The complete figure set (8 images) is available.)

secondaries. As promised, many of these settings display much larger velocity residuals than the primaries.

## ORCID iDs

Thomas R. Ayres https://orcid.org/0000-0002-1242-5124

## References

Ayres, T., De Pontieu, B., & Testa, P. 2021, ApJ, 916, 36
Ayres, T. R. 2010a, ApJS, 187, 149
Ayres, T. R. 2010b, in The 2010 STScI Calibration Workshop, ed. S. Deustua & C. Oliveira (Baltimore, MD: Space Telescope Science Institute), 7
Bainbridge, M., Barstow, M., Reindl, N., et al. 2017, Univ, 3, 32
Castelli, F., Cowley, C. R., Ayres, T. R., et al. 2017, A&A, 601, A119
Castelli, F., Kurucz, R. L., & Cowley, C. R. 2015, A&A, 580, A10
Chayer, P., Dixon, W. V., Fullerton, A. W., et al. 2015, MNRAS, 452, 2292
Cowley, C. R., Ayres, T. R., Castelli, F., et al. 2016, ApJ, 826, 158
Denes Couto, J. 2017, PhD thesis, The Catholic Univ. of America
France, K., Loyd, R. O. P., Youngblood, A., et al. 2016, ApJ, 820, 89
Gallenne, A., Kervella, P., Evans, N. R., et al. 2018, ApJ, 867, 121
Hoadley, K., France, K., Arulanantham, N., et al. 2017, ApJ, 846, 6
Jenkins, E. B., & Wallerstein, G. 2017, ApJ, 838, 85

Keeney, B. A., Stocke, J. T., Danforth, C. W., et al. 2017, ApJS, 230, 6
Peterson, R. C., & Kurucz, R. L. 2015, ApJS, 216, 1
Richardson, N. D., Moffat, A. F. J., Gull, T. R., et al. 2015, ApJ, 808, 88
Roman-Duval, J., Jenkins, E. B., Williams, B., et al. 2019, ApJ, 871, 151
Sansonetti, C. J., Kerber, F., Reader, J., et al. 2004, ApJS, 153, 555
Sansonetti, C. J., & Nave, G. 2014, ApJS, 213, 28
Savage, B. D., Kim, T.-S., Fox, A. J., et al. 2017, ApJS, 232, 25
Siqueira-Mello, C., Spite, M., Barbuy, B., et al. 2016, JPhCS, 665, 012056
Welty, D. E., Lauroesch, J. T., Wong, T., et al. 2016, ApJ, 821, 118
Zachary, J., Redfield, S., Linsky, J. L., et al. 2018, ApJ, 859, 42